Monovalent selective electrodialysis: Modelling multi-ionic transport across selective membranes

Monovalent selective electrodialysis: Modelling multi-ionic transport across selective membranes

Danyal Rehman[a], Yvana D. Ahdab[a], John H. Lienhard V[a,*]

[a]*Rohsenow Kendall Heat Transfer Laboratory, Massachusetts Institute of Technology, Cambridge, MA 02139-4307, U.S.A*

Abstract

Monovalent selective electrodialysis (MSED) is a variant of conventional electrodialysis (ED) that employs selective ion exchange membranes to preferentially remove monovalent ions relative to divalent ions. This process can be beneficial when the divalent rich stream has potential applications. In agriculture, for example, a stream rich in calcium and magnesium is deemed beneficial for crops and can decrease the use of fertilizers that would otherwise need to be re-introduced to the source water prior to irrigation. MSED has been used for salt production, brine concentration, and irrigation. An experimentally validated computational model to predict its performance, however, is not available in the literature. The present work uses concepts from conventional ED modelling to build a high-resolution predictive model for the performance of MSED. The model was validated with over 32 experiments at different operating conditions and observed to fit the data to within 6% and 8% for two different types of membranes. All voltage predictions were within 10% of experiments conducted. The model was then used to predict permselectivity across different salinities and compositions. These values were extended to investigate the economic benefits of using MSED to save fertilizers for greenhouses across the U.S. Results showed an average of $4,991 saved per hectare when employing MSED technology. These values aligned with predictions from two previous techno-economic studies conducted investigating MSED for agriculture.

Keywords: groundwater desalination, monovalent selective electrodialysis, permselectivity, transport model, mineral recovery

D. Rehman, Y.D. Ahdab, and J.H. Lienhard V, "Monovalent selective electrodialysis: modelling transport in multi-ionic solutions across selective membranes," *Water Research,* online 22 April 2021, **199**:117171, 1 July 2021.

*Corresponding author.
Email address: lienhard@mit.edu

Nomenclature

Roman Symbols

A_m	Membrane area, m^2
C	Concentration, $mol \cdot m^{-3}$
D	Diffusion coefficient, $m^2 \cdot s^{-1}$
E	Donnan potential, V
$\mathscr{F}$	Faraday constant, $C \cdot mol^{-1}$
h	Channel height, m
i	Current density, $A \cdot m^{-2}$
J	Flux, $mol \cdot m^{-2} \cdot s^{-1}$
k_f	Mass transfer coefficient
L_j	Membrane ion permeability, $m \cdot s^{-1}$
L_w	Membrane water permeability, $s \cdot m^{-1}$
M	Molar mass, $mg \cdot mol^{-1}$
N_{cp}	Number of cell pairs
P	Permselectivity
Q	Volumetric flow rate, $m^3 \cdot s^{-1}$
r	Solute ratio
$\bar{r}$	Resistance
Re_D	Reynolds number
R	Universal gas constant, $J \cdot mol^{-1} \cdot K^{-1}$
S	Salinity
Sc	Schmidt number
Sh	Sherwood number
T	Transport number
t_{cu}	Integral counter ion transport number
t	Process time, s
V_{el}	Electrode potential, V
V_{stack}	Stack potential, V
z	Valence

Greek Symbols

π	Osmotic pressure, bar
σ	Spacer shadow effect
Φ	Electric potential, $V \cdot m^{-1}$

Subscripts

c	Concentrate
cu	Counter ion
d	Diluate
div	Divalent
f	Final
j	Ion species
lim	Limiting
m	membrane
mon	Monovalent
o,i	Initial
r	Rinse
s	Salt
w	Water

Superscripts

cp	Cell pair

Acronyms

AEM	Anion exchange membrane
CEM	Cation exchange membrane
ED	Electrodialysis
MSED	Monovalent selective electrodialysis
RO	Reverse osmosis
TDS	Total dissolved solids, $mg \cdot L^{-1}$

1. Introduction

Desalination can play a crucial role in ensuring that irrigation water quality requirements are met. The process involves the treatment of water through the removal of dissolved solids that would otherwise make the water source unsuitable for irrigation applications. Because water quality is central to crop growth, advanced agriculture sectors, such as hydroponics and greenhouses, have begun adopting reverse osmosis (RO), the most widely used desalination technology, to treat their brackish source water. This brackish water is primarily groundwater that contains a total dissolved solids (TDS) of 1,000-10,000 mg/L and various major ions, including Na^+, Mg^{2+}, Ca^{2+}, Cl^-, and SO_4^{2-} [Stanton et al., 2017]. RO reduces brackish water salinity and removes solutes that are both detrimental and beneficial to crops [Cohen et al., 2018]. Consequently, these nutrients must be added back to the desalinated water through fertilizer and/or blending with nutrient-rich brackish water.

Monovalent selective electrodialysis (MSED) may serve as an alternate technology to RO with greater potential of tailoring source water to irrigation needs. MSED is a variant of electrodialysis (ED) that uses monovalent selective ion exchange membranes to create a diluate stream rich in divalent ions that serve as nutrients for crops (Ca^{2+}, Mg^{2+}, SO_4^{2-}) and a concentrate stream rich in monovalent ions that are harmful to crops (Na^+,Cl^-) [Rehman et al., 20-24 Oct. 2019, Dubai, U.A.E]. To initiate separation, a potential difference is applied across the MSED stack that induces ion migration and transport (see Fig. 1). Positively charged ions move towards the negatively charged electrode (the cathode) and negatively charged ions move towards the positively charged electrode (the anode). MSED membranes use charge-based separation to preferentially remove monovalent ions relative to divalent ions. The cation exchange membranes (CEM) allow for the passage of monovalent cations and reject the passage of monovalent anions and divalent cations. Similarly, the anion exchange membranes (AEM) allow for the passage of monovalent anions and reject the passage of monovalent cations and divalent anions.

MSED offers four main advantages over RO in the treatment of irrigation water. First, the selective removal of solutes damaging to crops results in less required fertilizer and corresponding cost savings. Second, the high water recovery of MSED, which can exceed 90% for brackish solutions [Strathmann, 2010], leads to water savings and less brine volume for disposal and/or reuse. Third, the higher chemical and mechanical stability of MSED membranes increases their lifetime relative to RO by up to 4-5 years on average [Strathmann, 2010]. Therefore, MSED membranes need to be replaced less frequently than those of RO. Fourth, the reversal process in MSED is expected to increase fouling resilience relative to RO.

Although MSED has been used to concentrate sodium chloride for salt production in Japan since the 1960s, the technology has not been commercially deployed for brackish water desalination [Kawate et al., 1983]. Consequently, the market standard for monovalent selective ion exchange membranes is designed for higher salinity applications. MSED research has similarly prioritized brine concentration of seawater and concentrated seawater salinities for salt production [Saracco and Zanetti, 1994, Saracco, 1997, Luo et al., 2018] and nutrient recovery from wastewater streams [Zhang et al., 2012, Tran et al., 2014, Reig et al., 2018].

To the best of the authors' knowledge, no studies have developed an experimentally validated model for MSED that predicts

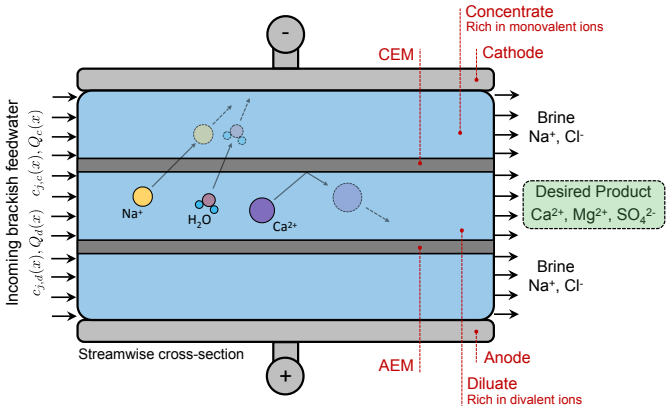

Figure 1: Monovalent selective electrodialysis working principles including one cell pair comprised of a CEM and an AEM, with groundwater as the feedwater. An applied voltage across the electrodes yields from the groundwater a concentrate stream for disposal and a high nutrient, low NaCl diluate stream for crop use. Similar behaviour to Ca^{2+} is exhibited by Mg^{2+}.

and optimizes performance for brackish water desalination. In the literature, only four experimental studies have investigated MSED performance in the brackish salinity range [Cohen et al., 2018, Jiang et al., 2019, Ahdab et al., 2020a, Rehman, 15 May 2020]. Cohen *et al.* [Cohen et al., 2018] found that the CSO/ASV membranes (Asahi Glass) remove 0.6 magnesium ions and 0.8 calcium ions for every sodium ion and the CMS/ACS Neosepta membranes (Astom Corporation) show divalent selectivity. Jiang *et al.* [Jiang et al., 2019] concluded that monovalent selectivity of the CR67 membranes (Suez Water Technologies & Solutions) for brackish waters can be significantly improved by including a polyethyleneimine coating layer on the membrane surfaces. The most recent two studies conducted by Ahdab *et al*. investigated the ion selectivity of the CMS/ACS Neosepta membranes and the Fujifilm Type 16 membranes for 16 brackish groundwater compositions [Ahdab et al., 2020a,b]. The findings suggest strong monovalent ion selectivity with a system capable of removing approximately 4 times the number of sodium ions for every calcium ion and approximately 7 times the number of sodium ions for every magnesium ion.

This paper extends conventional ED modelling techniques to develop an experimentally validated MSED process model that can predict MSED performance for any multi-ionic brackish feedwater. Because brackish groundwater ionic composition varies significantly with location, such a model may prove useful for greenhouses considering the implementation of MSED in place of RO. The model is tested and validated for over 32 MSED experiments carried out by Ahdab *et al.* [Ahdab et al., 2020a] on Neosepta's CMS/ACS membranes and Fujifilm's Type 16 membranes at various operating conditions typical of real-world systems [Ahdab et al., 2020b]. For a given feedwater, the model can predict the transport of various ions (Na^+, Mg^{2+}, Ca^{2+}, Cl^-, SO_4^{2-}) across the membranes and the membrane permselectivity towards monovalent ions. The model uncertainty is 6% and 8% of the Neosepta and Fujifilm experiments, respectively, based on a *t*-test at 95% confidence.

2. Model

2.1. Theory of transport

2.1.1. Ion and water molar balances

In modelling the MSED stack, the Nernst-Planck equations are used to quantify ion and water transport. The full form of the equations is provided by Eq. (1) and Eq. (2) for the cations and anions, respectively:

$$J_c = -D_c \nabla C_c - \frac{D_c z_c \mathscr{F}}{RT} C_c \nabla \Phi \tag{1}$$

$$J_a = -D_a \nabla C_a - \frac{D_a z_a \mathscr{F}}{RT} C_a \nabla \Phi \tag{2}$$

where J is the flux, D is the diffusion coefficient, C is the concentration, Φ is the electric potential, and z is the valence. Subscripts c and a denote the cations and anions, respectively. $\mathscr{F}$, R, and T are Faraday's constant, the universal gas constant, and temperature, respectively.

These equations can be simplified under the assumption of electroneutrality in the flow field and membranes. This provides an alternate formulation governed by transport numbers. The derivation is detailed in Appendix A. These transport numbers represent the current carried by a particular ion species as a proportion of the total applied current. The final form of these equations can be seen by Eq. (3) and Eq. (4) for ion and water transport, respectively. Although under brackish conditions, water transport is usually not modelled [Ortiz et al., 2005, Fidaleo and Moresi, 2005], in modelling multi-electrolyte solutions with lower concentrations of divalents, capturing the transport of water can play a role in characterizing transport.

$$J_j(x) = \frac{T_j^{cp} i}{z_j \mathscr{F}} - L_j \left[C_{j,c,m}(x) - C_{j,d,m}(x) \right] \tag{3}$$

$$J_w(x) = \left\{ \frac{T_w^{cp} i}{\mathscr{F}} + L_w \left[\pi_{j,c,m}(x) - \pi_{j,d,m}(x) \right] \right\} \frac{M_{\mathrm{H_2O}}}{\rho_{\mathrm{H_2O}}(x)} \tag{4}$$

where the first term on the right-hand side of Eq. (3) captures ion migration. In this term, T_j^{cp} is the transport number for a given chemical species j, i is the applied current density, and z_j is the ion valence. The second term in Eq. (3) accounts for diffusion of ion species, given the inherent differences in ionic concentrations across compartments. Here, L_j is the ion-specific permeability. The subscripts c, d, and m denote the concentrate, diluate, and membrane surface, respectively. In an MSED system, monovalent ions will accumulate in the concentrate compartment, creating a diffusive flux from the concentrate to the diluate. The opposite occurs for divalent ions as a result of the monovalent selectivity of the ion exchange membranes.

Similarly, in Eq. (4), T_w^{cp} is the transport number for the water. The first term on the right-hand side accounts for electro-osmosis of water molecules that move from the diluate stream into the concentrate compartment due to the bulk transport of ion species across compartments. The second term captures diffusion given the inherent concentration differences between the diluate and concentrate compartments. Here, π is the osmotic pressure and L_w is the water permeability. $M_{\mathrm{H_2O}}$ and $\rho_{\mathrm{H_2O}}(x)$ are the molar mass and density of water, respectively. The latter term varies as a function of salinity and is calculated at each streamwise point along the stack. Both equations are used to calculate J_j and J_w, the ion-specific flux and the water flux across the membrane at each spatial increment within the stack, respectively.

The Nernst-Planck equations intrinsically neglect any kinetic coupling that may be present in the solution between chemical species. However, previous studies extending the Nernst-Planck equations to high salinity applications have shown agreement between experiments and the potential of Nernst-Planck equations in predicting transport characteristics [McGovern et al., 2014, Fidaleo and Moresi, 2005]. Tests conducted by McGovern *et al.* have shown alignment between models and experiments to salinities up to 200 g/kg of NaCl [McGovern et al., 2014]. Therefore, at the low concentrations (up to 10 g/kg TDS), at which the stack is to be characterized for in the brackish range, errors are assumed to be negligible.

The transport equations previously stated in Eq. (3) and Eq. (4) are solved at different spatial increments within the MSED stack. The stack is discretized into differential volumes as seen in Fig. 2.

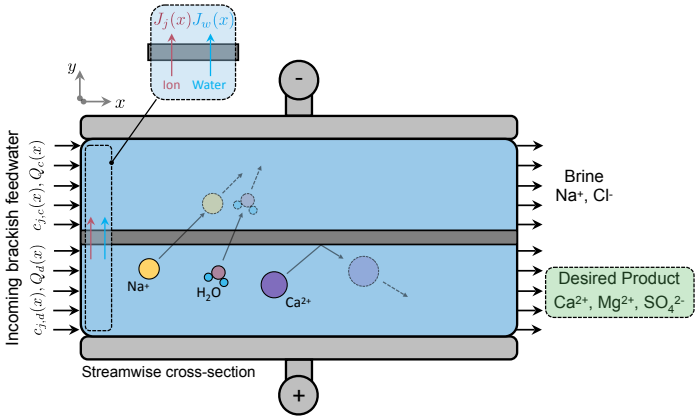

Figure 2: Discretized MSED stack with ion and water flux direction conventions defined (for one cation exchange membrane). Q_d and Q_c represent the volumetric flow rate of water into the diluate and concentrate compartments, respectively. The diluate yields the desired product stream rich in divalent ions while the concentrate yields a brine stream rich in adverse monovalent ions.

The flux is calculated at the membrane interface for each spatial location and integrated. One equation for water transport and another equation for each ion species is required to quantify transport out of the diluate stream. The same relations apply to the concentrate stream for conservation. These are provided by Eq. (5) and Eq. (6):

$$\frac{dQ_d}{dA_m} = -\frac{dQ_c}{dA_m} = -N_{cp} J_w(x) \tag{5}$$

$$\frac{d(C_{j,d} Q_d)}{dA_m} = -\frac{d(C_{j,c} Q_c)}{dA_m} = -N_{cp} J_j(x) \tag{6}$$

where Q is water's volumetric flow rate, C_j is the concentration of ion species j, A_m is the membrane area, and N_{cp} is the number of cell pairs. Subscripts c and d denote the concentrate and diluate, respectively. In addition, $dA_m = h dx$, where h is the channel height and dx is the differential change in position in the streamwise direction of the MSED stack. Eq. (5) and Eq. (6) can be combined to give the final forms of the transport equations:

$$\frac{dC_{j,d}}{dx} = \frac{hN_{cp}}{Q_d(x)}\left[C_{j,d}(x)J_w(x) - J_j(x)\right] \tag{7}$$

$$\frac{dC_{j,c}}{dx} = -\frac{hN_{cp}}{Q_c(x)}\left[C_{j,c}(x)J_w(x) - J_j(x)\right] \tag{8}$$

$$\frac{dQ_d}{dx} = -hN_{cp}J_w(x) \tag{9}$$

$$\frac{dQ_c}{dx} = hN_{cp}J_w(x) \tag{10}$$

The derivation of Eq. (7) and Eq. (8) is provided in Appendix B. To solve these differential equations, the integration is performed using a 4$^{\text{th}}$ order adaptive Runge-Kutta-Fehlberg (RKF) scheme for increased accuracy and decreased computational expense [Chapra and Canale, 2010]. The boundary condition required for these sets of equations are: $Q_d(x=0) = Q_0$, $Q_c(x=0) = Q_0$, $c_{j,d}(x=0) = c_{j,0}$, and $c_{j,c}(x=0) = c_{j,0}$.

Mesh-independence studies are performed on the numerical model to determine a balance between computational cost and model accuracy (Appendix C).

2.1.2. Limiting current density and hydrodynamics

The limiting current density is defined as the value of current above which water molecules begin to dissociate. In multi-ionic solutions, instead of splitting water, any current in excess of the limiting current density accelerates the transport of other ionic species. For MSED in particular, this can be detrimental and lead to worsened permselectivity. The limiting current density in this work is re-defined for each individual ion species using Eq. (11):

$$i_{\text{lim},j} \equiv \frac{D_j z_j \mathscr{F} \delta}{T_j^{cp} - t_{\text{cu},j}} C_{j,d,b} = \frac{D_j z_j \mathscr{F}}{T_j^{cp} - t_{\text{cu},j}}\left(\frac{2h}{\text{Sh}}\right) C_{j,d,b} \tag{11}$$

where Sh is the Sherwood number, $t_{\text{cu},j}$ is the integral counter-ion transport number of species j, δ is the boundary layer thickness, and $C_{j,d,b}$ is the concentration of species j in the bulk of the diluate compartment. δ can be expressed as a function of the channel height and Sherwood number using the stagnant film model [Zydney, 1997]. The stagnant film model used in the model formulation has shown alignment with experiments at 200 g/kg, and therefore, errors are assumed to be negligible within the low concentration ranges presented in this work. To calculate the Sherwood number, the correlation provided in Eq. (12) has been previously employed and validated by McGovern *et al.* for their system [McGovern et al., 2014]. The current experimental setup used is a modification of their setup, where the conventional ED membranes have been replaced with monovalent selective membranes from Neosepta and Fujifilm [Ahdab et al., 2020a,b, 2021]. The experimental setup used in this work is described in Appendix D. The correlations proposed show alignment to within 10% of experiments [Kuroda et al., 1983].

$$\text{Sh} = 0.37\text{Re}^{1/2}\text{Sc}^{1/3} \tag{12}$$

Here, Re is the Reynolds number and Sc is the Schmidt number. The Reynolds number is calculated at each spatial point along the stack using the local velocity, hydraulic diameter, and salinity-dependent densities and viscosities. Despite the water composition varying along the stack, a bulk salinity is used in determining the density and dynamic viscosity of the solution at these points using relations provided by Nayar *et al.* [Nayar et al., 2016]. Diffusion coefficients for each ion species in water are obtained from studies conducted by Sato *et al.* [Sato et al., 1996]. $t_{\text{cu},j}$ is determined for each ion using Eq. (13) in line with conventional ED modelling methods:

$$t_{\text{cu},j} = \frac{z_j D_j C_j}{\sum_{i=1}^{N_i} z_i D_i C_i} \tag{13}$$

where N_i represents the total number of ions in the solution.

In an ideal MSED system, there is no transport of divalent ions, and only the transport of monovalent ions. However, even in the presence of a non-ideal system, the transport of monovalent ions is expected to significantly outweigh the transport of divalent ones [Ahdab et al., 2020b]. Therefore, the denominator in Eq. (11) is expected to be far smaller for divalent ions, leading to larger limiting current densities. For this reason, it can be assumed with a relatively high degree of confidence that the bottleneck in the limiting current density is primarily governed by the transport of monovalent ions in the solution. This assumption is later validated by our experiments, in which the ratio of transport numbers between the monovalent sodium and the divalent calcium and magnesium is at least 3.5 in all conducted experiments.

2.1.3. Concentration polarization

Concentration polarization (CP) leads to concentration gradients that can adversely impact transport, and subsequently the desalination process. Accounting for CP is critical as modelling errors due to its neglection can be on the order of 15-20% [Kuroda et al., 1983].

The stagnant film model used in this work was previously validated by McGovern *et al.* and Cheheyab *et al.* [McGovern et al., 2014, Chehayeb et al., 2017]. The model states:

$$\Delta C_j = \left(\frac{T_j^{cp} - t_{\text{cu},j}}{D_j}\right)\left(\frac{i}{z_j \mathscr{F}}\right)\left(\frac{2h}{\text{Sh}}\right) \tag{14}$$

where ΔC_j is the difference in concentration between the bulk flow and the membrane interface. Eq. (14) can be incorporated into the transport equations from Section 2.1.1 as seen:

$$J_j(x) = \frac{T_j^{cp} i}{z_j \mathscr{F}} - \underbrace{L_j\left(\left[C_{j,c,b}(x) + \Delta C_j\right] - \left[C_{j,d,b}(x) - \Delta C_j\right]\right)}_{\text{modified ion diffusion term}} \tag{15}$$

$$J_w(x) = \frac{T_w^{cp} i}{\mathscr{F}} + \underbrace{L_w\left[\pi_{j,c,m}(C_{j,c,b}(x) + \Delta C_j) - \pi_{j,d,m}(C_{j,d,b}(x) - \Delta C_j)\right]}_{\text{modified water osmosis term}} \tag{16}$$

where the subscript b denotes the bulk flow. The concentration difference between the diluate and concentrate compartments is equal in size based on mass conservation (i.e. $\Delta C_{j,c} = \Delta C_{j,d} = \Delta C_j$).

2.1.4. Modelling MSED as a circuit

One of the most commonly employed models for conventional ED is a circuit composed of resistors and voltage sources. Fig. 3 presents a cross section of the MSED stack where each resistance and voltage source is shown for one cell pair in the circuit.

The mathematical representation of the entire stack is:

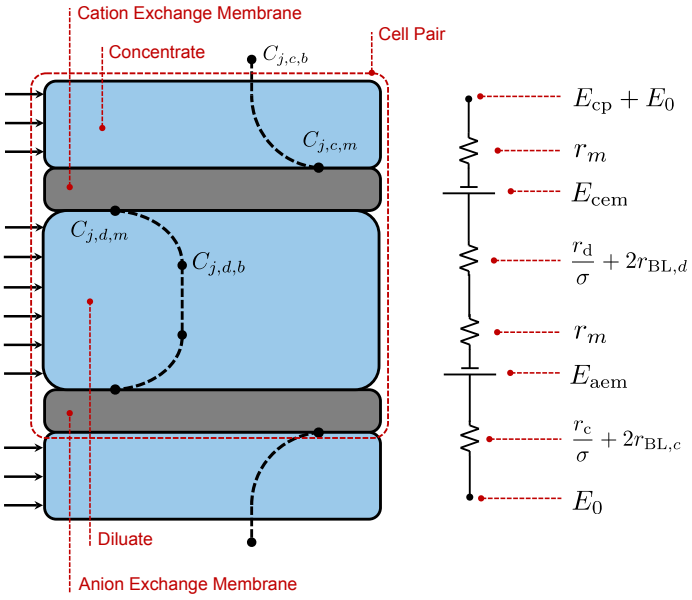

Figure 3: Decomposing one cell pair of the MSED stack into ohmic resistances and Donnan potentials. Resistances occur in the diluate and concentrate streams as well as the cation and anion exchange membranes.

$$E_{stack} = i\left[N_{cp}\left(2\bar{r}_m + \frac{\bar{r}_d}{\sigma} + \frac{\bar{r}_c}{\sigma} + 2\bar{r}_{BL,d} + 2\bar{r}_{BL,c}\right) + \bar{r}_m + 2\bar{r}_r\right] + N_{cp}\left(E_{aem} + E_{cem}\right) + E_{el} \quad (17)$$

where E_{el} and E_{stack} are the potential differences across the electrodes and the entire MSED stack, respectively. Subscripts m, d, c, BL, and r denote the membranes, diluate, concentrate, boundary layer, and electrode rinse, respectively. E_{aem} and E_{cem} are the Donnan potentials induced by concentration differences of each ion species on either side of the membrane. Lastly, σ accounts for the shadow spacer effect.

Fixed values for membrane resistances are usually quoted by membrane manufacturer; however, the values inherently vary as a function of salinity. Membrane characterization tests have been previously conducted on the set of Neosepta and Fujifilm membranes used in this work by Ahdab *et al.* [Ahdab et al., 2020a,b]. The characterization studies and best fit curves for both membranes are provided in Appendix E[1]. Local stack data was interpolated to calculate membrane resistance at each spatial increment in the stack.

The shadow spacer effect was also experimentally determined for both sets of membranes in the aforementioned work for 3 different applied current densities (18, 22, and 31 A/m^2) [Ahdab et al., 2020a,b]. This yielded a shadow spacer effect term of $\sigma = 0.72 \pm 0.09$. A value of 0.72 was assumed during all modelling studies conducted.

The diluate and concentrate resistances are determined based on the Onsager and Falkenhagen equations [Kortüm, 1965]:

$$\bar{r}_d + \bar{r}_c = \frac{h}{\Lambda_d(C_{d,b})C_{d,b}} + \frac{h}{\Lambda_c(C_{c,b})C_{c,b}} \quad (18)$$

[1]The membrane resistances for both the cation exchange membrane and the anion exchange membrane are assumed to be equal.

where Λ represents the molar conductivity of the solution and is intrinsically a function of concentration. The concentrations used to calculate these ohmic resistances are the bulk values of the diluate and concentrate. The Falkenhagen equations have been validated in the concentration ranges being used in the model [Wright et al., 2018a, Shah et al., 2018]. For all the relevant salts, the molar conductivities have been compiled and plotted as a function of concentration in Appendix F. The same approach is used to calculate the resistance of the electrode rinse assuming sodium sulphate with a constant and time-invariant concentration of 0.2 M.

The ohmic diluate and concentrate resistances calculated above determine the resistance of the bulk solution; however, they fail to capture the resistance within the boundary layers that result from CP. A $\bar{r}_{BL}$ term is subsequently introduced to Eq. (17) to account for these effects. This approach introduces two boundary layer resistances – one for the diluate compartment and one for the concentrate compartment:

$$\bar{r}_{BL,d} = \frac{\delta}{\Lambda_{BL}\left(\frac{C_{d,b}+\Delta C_j}{2}\right)\left[\frac{C_{d,b}+\Delta C_j}{2}\right]} \quad (19)$$

$$\bar{r}_{BL,c} = \frac{\delta}{\Lambda_{BL}\left(\frac{C_{c,b}+\Delta C_j}{2}\right)\left[\frac{C_{c,b}+\Delta C_j}{2}\right]} \quad (20)$$

The electrode potential difference, E_{el}, is usually between 1.5 and 3 V for standard ED electrodes in the literature [Wright et al., 2018b, Ortiz et al., 2005, Wright and Winter, 2014]. A value of 2 V is assumed in this work. The value was varied during the course of the model validation process and the model was found to be insensitive to deviations in the parameter.

The Donnan potentials can be expressed as a function of ion-specific transport characteristics [McGovern et al., 2014, Chehayeb et al., 2017]. The mathematical representation is seen in Eq. (21):

$$E_{aem} + E_{cem} = \left[\sum_{i=1}^{N_{ions}} \frac{T_j^{cp}}{z_j \mathscr{F}}\left(\mu_{j,c,m} - \mu_{j,d,m}\right)\right] + \frac{T_w^{cp}}{\mathscr{F}}\left(\mu_{w,c,m} - \mu_{w,d,m}\right) \quad (21)$$

where μ is the chemical potential. The chemical potential of a given ion species or water can be determined based on a standard reference state and the activity of the ion species as shown below:

$$\mu_j = \mu_j^\circ + RT\ln\left(a_j\right) = \mu_j^\circ + RT\ln\left(\gamma_j b_j\right) \quad (22)$$

where a_j is the activity of ion species j. The activity can be rewritten as a product of γ_j, the activity coefficient, and b_j, the molality. μ_j° refers to the reference chemical potential of chemical species j – a well tabulated value in the literature for many ion species [Harvie and Weare, 1980]. The reference state chemical potential of relevant species is provided in Appendix G.

2.1.5. *Pitzer-Kim theory for mixed electrolytes*

We apply the Pitzer-Kim model [Pitzer, 1973, Pitzer and Mayorga, 1973, 1974, Pitzer and Kim, 1974, Pitzer, 1975] to evaluate the activity coefficient of each ion, γ_i, and the osmotic coefficient for water, ϕ. The method has shown strong alignment with experimental data. This formulation forms the basis of the MSED stacks voltage and resistance calculations. The Pitzer-Kim model decomposes the excess Gibbs free energy into a virial expansion that is truncated after the

third term [Pitzer, 1973]. The expansion for a given cation is:

$$\ln\gamma_M = z_M^2\mathfrak{F} + \sum_{a=1}^{N_a} b_a(2B_{Ma} + ZC_{Ma}) + \sum_{c=1}^{N_c} b_c(2\phi_{Mc} + \sum_{a=1}^{N_a} b_a\psi_{Mca}) + \sum_{a=1}^{N_a-1}\sum_{a'=a+1}^{N_a} b_a b_{a'}\psi_{aa'M} + |z_M|\sum_{c=1}^{N_c}\sum_{a=1}^{N_a} b_c b_a C_{ca} + \sum_{n=1}^{N_n} b_n(\lambda_{nM}) \tag{23}$$

Similarly, for an anion in solution:

$$\ln\gamma_X = z_X^2\mathfrak{F} + \sum_{c=1}^{N_c} b_c(2B_{Xc} + ZC_{Xc}) + \sum_{a=1}^{N_a} b_a(2\phi_{Xa} + \sum_{c=1}^{N_c} b_c\psi_{Xca}) + \sum_{c=1}^{N_c-1}\sum_{c'=c+1}^{N_c} b_c b_{c'}\psi_{cc'X} + |z_X|\sum_{c=1}^{N_c}\sum_{a=1}^{N_a} b_c b_a C_{ca} + \sum_{n=1}^{N_n} b_n(\lambda_{nX}) \tag{24}$$

Lastly, the osmotic coefficient of the solution is given by:

$$\begin{aligned}\frac{1}{2}\sum_{i=1}^{N_s} b_i(\phi-1) = {} & \frac{-A^\phi\sqrt{I^3}}{1+1.2\sqrt{I}} + \sum_{c=1}^{N_c}\sum_{a=1}^{N_a} b_c b_a(B^\phi_{MX} + ZC_{ca}) \\ & + \sum_{c=1}^{N_c-1}\sum_{c'=c+1}^{N_c} b_c b_{c'}(\Phi^\phi_{cc'} + \sum_{a=1}^{N_a} b_a\psi_{cc'a}) \\ & + \sum_{a=1}^{N_a-1}\sum_{a'=a+1}^{N_a} b_a b_{a'}(\Phi^\phi_{aa'} + \sum_{c=1}^{N_c} b_c\psi_{aa'c}) \\ & + \sum_{n=1}^{N_n}\sum_{a=1}^{N_a} b_n b_a\lambda_{na} + \sum_{n=1}^{N_n}\sum_{c=1}^{N_c} b_n b_c\lambda_{nc}\end{aligned} \tag{25}$$

where the subscript s denotes all solutes (includes cations, anions, and neutrals). In addition, $\mathfrak{F}$ is a function of ionic strength, I, and is described by the following equation:

$$\begin{aligned}\mathfrak{F} = {} & -A^\phi\left(\frac{\sqrt{I}}{1+1.2\sqrt{I}} + \frac{1}{1.2}\ln(1+1.2\sqrt{I})\right) + \sum_{c=1}^{N_c}\sum_{a=1}^{N_a} b_c b_a B'_{ca} \\ & + \sum_{c=1}^{N_c-1}\sum_{c'=c+1}^{N_c} b_c b_{c'}\Phi'_{cc'} + \sum_{a=1}^{N_a-1}\sum_{a'=a+1}^{N_a} b_a b_{a'}\Phi'_{aa'}\end{aligned} \tag{26}$$

where A^ϕ is one-third of Debye's limiting gradient and a simplification of the Pitzer-Kim model. The value of A^ϕ evaluates to approximately 0.3903 at standard conditions[2]. Using only the A^ϕ term provides accuracy at low concentrations but fails to capture the non-idealities of the solution at higher concentrations where short range interactions are of increasing importance. Subscripts M, X, and N denote the cations, anions, and neutrals, respectively. Similar definitions apply to c, a, and n. N_c, N_a, and N_n are the total number of cations, anions, and neutrals in the solution, respectively. Lastly, z is the valence and b is the molality of a given species. The remaining terms present in the equations represent binary and ternary interaction parameters and virial coefficients that can be determined using the mathematical expressions provided in Appendix G.

[2] A^ϕ is a function of density, temperature, and other constants (Faraday's constant, the dielectric constant, Avogadro's constant, and the universal gas constant.) Density corrections, as stated previously, are taken from correlations provided by Nayar *et al.* [Nayar et al., 2016].

2.2. Parameter regression and permselectivity

In experimentally conducted studies to determine transport numbers, tests are performed at constant current. The change in mass of the ions and solution are measured over a fixed amount of time. It is assumed that diffusion does not play a role at this time scale. Therefore, the transport equations are rearranged and integrated through time to calculate transport numbers as seen by Eq. (27) and Eq. (28):

$$T_j^{cp} = \frac{\Delta w_j\mathscr{F}}{i\Delta t A_m N_{cp}} \tag{27}$$

$$T_w^{cp} = \frac{\Delta w_{w,d}\mathscr{F}}{i\Delta t A_m N_{cp} M_{\mathrm{H_2O}}} \tag{28}$$

where Δw_j and $\Delta w_{w,d}$ are the changes in weight of the ions and water after time Δt, respectively. McGovern *et al.* and Ahdab *et al.* have performed similar experiments to calculate transport numbers previously [Ahdab et al., 2020a,b, McGovern et al., 2014].

For membrane diffusion permeabilities, tests are conducted at zero applied current with diffusion being the only mechanism of transport. The transport equations then neglect the migration and electromigration terms and are rearranged to calculate ion-specific diffusion permeabilities and water permeabilities of the membranes as seen by Eq. (29) and Eq. (30):

$$L_j = \frac{\Delta m_j/M_j}{\left(C_{j,c} - \frac{\Delta C_{j,d}}{2}\right)\Delta t A_m N_{cp}} \tag{29}$$

$$L_w = \frac{\Delta m_{w,d}/M_{\mathrm{H_2O}}}{(\pi_c - \pi_d)\Delta t A_m N_{cp}} \tag{30}$$

where M_j is the molar mass of ion species j, $C_{j,c}$ is the concentration of ion species j in the concentrate, and $C_{j,d}$ is the concentration of ion species j in the diluate. In addition, π_c and π_d are the osmotic pressures of the concentrate and diluate, respectively. McGovern *et al.* and Ahdab *et al.* have performed similar experiments in previous work [Ahdab et al., 2020a,b, McGovern et al., 2014].

For higher salinities or multi-ionic solutions, this approach may introduce errors due to the pronounced effects of back diffusion under these conditions. To calibrate the model, the transport numbers and membrane diffusion permeabilities are used as model fitting parameters. 26 experiments over 16 brackish groundwater compositions for 2 different sets of membranes served as model calibration inputs. In addition, 3 operating applied current densities: 0.2 i/i_{lim}, 0.5 i/i_{lim}, and 0.8 i/i_{lim} are also tested throughout the model validation process to characterize the system operating space [3]. Concentrations of each ion species were measured frequently enough to ensure 4-5 data points for each composition and salinity for all conducted tests. The compositions tested are provided in Table 1.

A normalized L^2 norm between the models prediction of concentration and voltage as a function of time and the experimental output is minimized for all these cases to determine accurate ion-specific transport numbers and membrane diffusion permeabilities. A single

[3] The applied current density ratios i/i_{lim} stated refer to those observed at the end of each experiment. These values correspond to the lowest concentration, and consequently, the lowest limiting current density seen by the stack during a given experiment.

Table 1: Water compositions tested in MSED experiments. Four different salinities are tested for each composition: 1,500, 3,000, 5,000, and 10,000 mg/L along with the water composition run by Cohen *et al.* [Cohen et al., 2018] (corresponds to Comp. 4). The ratios, r_j, correspond to divalent ion solute ratios as defined by Ahdab *et al.* [Ahdab et al., 2020a].

Water	$r_{Ca^{2+}}$	$r_{Mg^{2+}}$	$r_{SO_4^{2-}}$	TDS
Comp. 1	0.32	0.08	0.40	1,500-10,000
Comp. 2	0.46	0.14	0.14	1,500-10,000
Comp. 3	0.13	0.09	0.64	1,500-10,000
Comp. 4	0.14	0.08	0.30	2,588

objective genetic algorithm is used as the optimization method to determine the global minimum. The objective function and pertinent constraints are seen in Eq. (31). A constraint is imposed to ensure that the sum of the transport numbers for both cations and anions to be less than or equal to 2 in alignment with their definition.

$$\begin{aligned} \min_{T_j^{cp},L_j,T_w^{cp},L_w} \quad & \sum_{i=1}^{N_{\text{ions}}} \left[\left(\frac{C_{i,\text{model}} - C_{i,\text{exp}}}{C_{i,\text{model}}} \right)^2 + \left(\frac{E_{\text{stack,model}} - E_{\text{stack,exp}}}{E_{\text{stack,model}}} \right)^2 \right] \\ \text{s.t.} \quad & \sum_{j=1}^{N_{\text{cations}}} T_j^{cp} \leq 1 \\ \text{s.t.} \quad & \sum_{j=1}^{N_{\text{anions}}} T_j^{cp} \leq 1 \end{aligned} \tag{31}$$

Upon quantification of the transport numbers and permeabilities, a permselectivity can be defined, as seen by Eq. (32). The permselectivity serves as the metric in quantifying the preferential removal of divalent ion species with respect to monovalent ions.

$$P_{\text{mon}}^{\text{div}} \equiv \frac{T_{\text{div}}/w_{\text{div},0}}{T_{\text{mon}}/w_{\text{mon},0}} \tag{32}$$

Here, P is the permselectivity and the 0 in the subscript denotes measurements at $t = 0$. The subscripts 'div' and 'mon' denote divalent species and monovalent species, respectively. As P tends to unity, the monovalent selectivity of the membranes' decreases. In other words, a smaller permselectivity represents better rejection of monovalent ions with respect to divalent ions. Consequently, lower values of permselectivity are more desirable for efficient MSED systems.

3. Results and discussion

3.1. Fitted ion transport numbers and membrane diffusion permeabilities

Table 2 and 3 below show the average values of transport numbers and permeabilities determined through the minimization procedure for both the Neosepta and Fujifilm membranes, respectively. Comparisons to the literature are also provided [Ahdab et al., 2020a,b]. Ion and water transport numbers are dimensionless while ion and water permeabilities are in m s^{-1} and mol m^{-2} s^{-1} bar^{-1}, respectively.

The transport numbers obtained through the regression tend to be equal to or larger than those experimentally determined by Ahdab *et al.* [Ahdab et al., 2020a]. This is because the effects of diffusion and concentration polarization are accounted for by the model

Table 2: Transport numbers and permeabilities for the Neosepta membranes regressed from experiments. These results correspond to average values obtained across concentrations ranging from 1,500-10,000 mg/L for Comp. 1 to Comp. 4. Comparisons included to bench-scale tests conducted in the lab by Ahdab *et al.* [Ahdab et al., 2020a].

Ions	T (mod)	T (exp)	L (mod)	L (exp)
Na^+	0.42	0.39	3.0×10^{-8}	3.1×10^{-8}
Ca^{2+}	0.11	0.10	4.9×10^{-9}	4.7×10^{-9}
Mg^{2+}	0.02	0.02	3.8×10^{-9}	3.5×10^{-9}
Cl^-	0.51	0.48	3.1×10^{-8}	3.1×10^{-8}
SO_4^{2-}	0.06	0.05	6.6×10^{-9}	6.7×10^{-9}
H_2O	9.8	-	3.3×10^{-4}	-

Table 3: Ion transport numbers and permeabilities for the Fujifilm membranes regressed from experiments. These results correspond to average values obtained across concentrations ranging from 1,500-10,000 mg/L for Comp. 1 to Comp. 4. Comparisons included to bench-scale tests conducted in the lab by Ahdab *et al.* [Ahdab et al., 2020b].

Ions	T (mod)	T (exp)	L (mod)	L (exp)
Na^+	0.57	0.55	3.3×10^{-8}	3.4×10^{-8}
Ca^{2+}	0.09	0.09	4.2×10^{-9}	4.3×10^{-9}
Mg^{2+}	0.01	0.01	3.4×10^{-9}	3.2×10^{-9}
Cl^-	0.55	0.53	3.2×10^{-8}	3.3×10^{-8}
SO_4^{2-}	0.04	0.04	6.3×10^{-9}	6.2×10^{-9}
H_2O	9.5	-	3.5×10^{-4}	-

and therefore, the migratory flux passing through the membrane in actuality is higher than the values traditionally calculated from experimental results, which are obtained by neglecting these effects. When the standard calculation methods using Eq. (27) and Eq. (29) were input into the model, 5-7% increases appeared in the ion flux. Consequently, transport numbers determined by the traditional reduction of experimental data can be seen as lower bounds.

The transport numbers of the water determined through the minimization were 9.8 and 9.5 for the Neosepta and Fujifilm membranes, respectively. These align with values obtained in the literature for conventional ED experiments, which quote values between 6-11 for salinities up to 200 g/kg [McGovern et al., 2014]. Lower concentrations tend to have higher water transport numbers with values between 10-11 in the brackish water range that monotonically decrease as a function of salinity [McGovern et al., 2014]. A similar argument as with ion transport numbers explains the transport number ranges seen for water. The only difference is, for water, the diffusive flux works in the same direction as the electro-migratory flux, leading to lower values of water transport numbers for the same total water flux. Consequently, the transport numbers obtained through a data reduction process that neglects the diffusive and electro-migratory effects are higher than the actual water transport numbers. In addition, for MSED in comparison to conventional ED, multi-ionic solutions have been seen to hinder water transport, further contributing to the reduced water transport numbers calculated. This is in line with the observations noted in literature [Ahdab et al., 2020a,b, McGovern et al., 2014].

The ion and water permeabilities calculated show no distinct trend but are in agreement with experimental values. The permeabilities of the divalent ions appear to be nearly an order of magnitude

smaller than those of the monovalent ions. This difference is expected owing to the preferential removal of monovalent ions within the MSED stack. In addition, the water permeabilities of the MSED membranes: 3.3×10^{-4} mol m^{-2} s^{-1} bar^{-1} and 3.5×10^{-4} mol m^{-2} s^{-1} bar^{-1}, are both seen to be in agreement with those obtained for conventional ED membranes: 2.5-3 $\times 10^{-4}$ mol m^{-2} s^{-1} bar^{-1} in the brackish water range [McGovern et al., 2014].

Lastly, both the ion transport numbers and ion permeabilities of monovalent species are larger for the Fujifilm membranes in comparison to the Neosepta membranes. Simultaneously, the divalent ion transport numbers and ion permeabilities are lower for the Fujifilm membranes. This difference shows the better monovalent selectivity of the Fujifilm membranes relative to the Neosepta membranes. The comparison between the permselectivity of the two sets of membranes is explored in more detail for all conducted modelling studies in Section 3.4.

3.2. *Transient concentration fits*

The model is validated against 26 experiments run in the lab at different input compositions and salinities in the brackish water range [Ahdab et al., 2020a,b]. An additional 6 were run at different applied current densities to fully characterize the operating space for the MSED system. Using the individual ion and water transport numbers along with ion and water permeabilities shown in Section 3.1, transient concentration profiles are calculated. Fig. 4(a) through 4(d) and Fig. 5(a) through Fig. 5(d) show the agreement between the model and the experiments for four different salinities at a set input composition for the Neosepta and Fujifilm membranes, respectively.

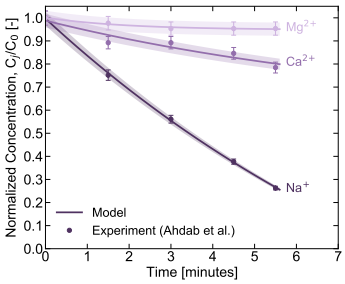

(a) Input feedwater of 1,500 ppm with Comp. 2 using Neosepta's CMS/ACS membranes [Ahdab et al., 2020a].

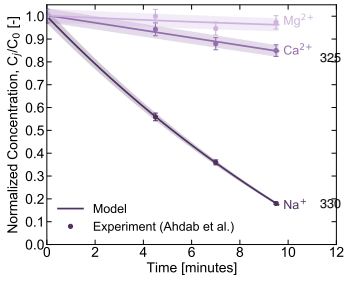

(b) Input feedwater of 3,000 ppm with Comp. 2 using Neosepta's CMS/ACS membranes [Ahdab et al., 2020a].

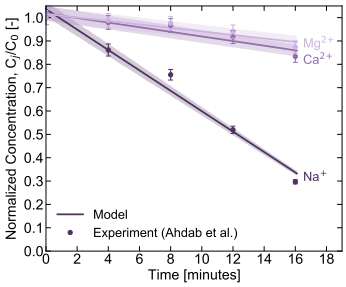

(c) Input feedwater of 5,000 ppm with Comp. 2 using Neosepta's CMS/ACS membranes [Ahdab et al., 2020a].

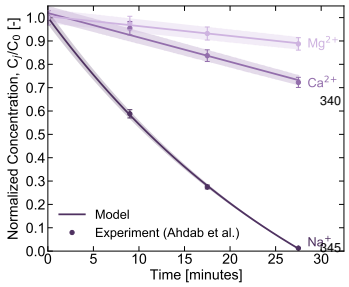

(d) Input feedwater of 10,000 ppm with Comp. 2 using Neosepta's CMS/ACS membranes [Ahdab et al., 2020a].

Figure 4: Concentration profiles of each ion species for different input feedwater compositions using the Neosepta CMS/ACS membranes [Ahdab et al., 2020a].

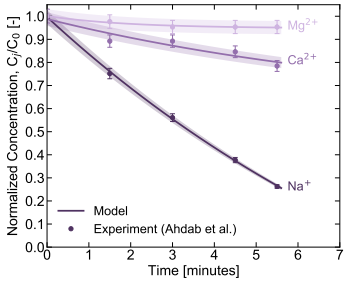

(a) Input feedwater of 1,500 ppm with Comp. 2 using Fujifilm's Type 16 membranes [Ahdab et al., 2020b].

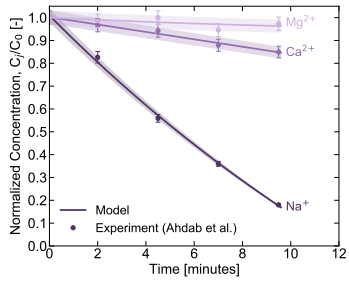

(b) Input feedwater of 3,000 ppm with Comp. 2 using Fujifilm's Type 16 membranes [Ahdab et al., 2020b].

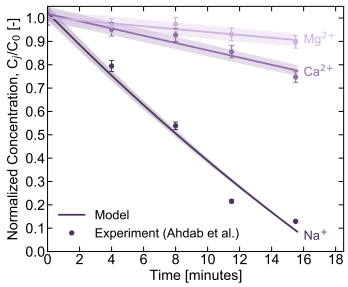

(c) Input feedwater of 5,000 ppm with Comp. 2 using Fujifilm's Type 16 membranes [Ahdab et al., 2020b].

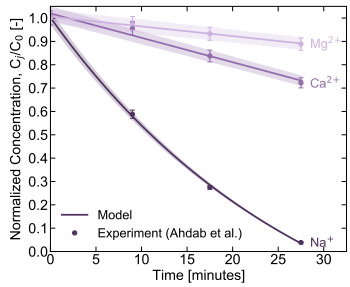

(d) Input feedwater of 10,000 ppm with Comp. 2 using Fujifilm's Type 16 membranes [Ahdab et al., 2020b].

Figure 5: Concentration profiles of each ion species for different input feedwater compositions using the Fujifilm Type 16 membranes [Ahdab et al., 2020b].

The primary y-axis on the curves is the concentration of a given ion species after it has been normalized by its initial concentration. The x-axis represents the duration of the experiments. The desalination process is carried out until the sodium level in the diluate tank is below the requirements for irrigation use. At this point, approximately 80-90% of the sodium has been removed from the entering streams. In addition, all conducted studies, the stack consistently operates below a final applied current density that is equal to 70% of the limiting current density ($i/i_{\text{lim}} = 0.7$).

The curvature and deviation from linearity present in the transient concentration trends arises from the increasing diffusive flux across the membranes over time. The diffusion of ions across compartments decelerates the overall transport for a fixed migratory flux based on Eq. (3) and Eq. (4). This hindrance in transport is represented by the decreasing gradient in the normalized concentration profiles of all observed ion species. The model shows good agreement with all experiments conducted with an uncertainty of 8% using a t-statistic at a 95% confidence limit for the Fujifilm membranes. Similarly, for the Neosepta membranes, an uncertainty of 6% is observed using the same statistical measure.

During the desalination process, the ion flux due to migration dominates the diffusive flux. The ion migration term is nearly 2 orders of magnitude larger than the diffusive flux for all ions tested. Similarly, for water, the electroosmosis term is nearly one order of magnitude larger than the osmosis term. The curvature present in the transient concentration profiles is also seen to be more pronounced for higher salinities. This difference results from the relatively large diffusive fluxes observed when the differences in concentrations between the diluate and concentrate compartment are large during the

desalination process.

The alignment between the model and experiments speaks to the models predictive capabilities for a set of a membranes in the brackish water range. However, since the governing transport equations are directly a function of applied current density, to fully characterize system performance, the applied voltage across the stack also needs to be modelled (Section 3.3).

3.3. Stack voltage distributions

In all conducted experiments, the stack voltage was recorded as a function of time for both sets of membranes. The model was used to predict the average voltage across the stack at any given point in time using Eq. (17). Alignment between the model and experiments is shown in Fig. 6(a) to Fig. 6(d) for the Neosepta and Fujifilm membranes. The blue data points represent the Fujifilm membranes and the burgundy data points represent the Neosepta membranes.

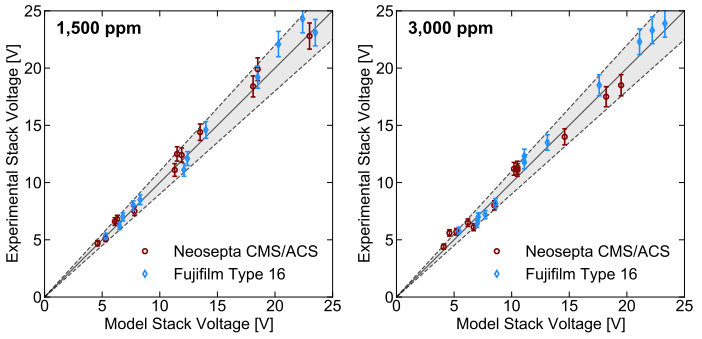

(a) Model predictions of stack voltage against experimental stack voltage for 1,500 ppm input feedwater and all tested compositions sampled at 3-5 points in time for both Fujifilm and Neosepta membranes.

(b) Model predictions of stack voltage against experimental stack voltage for 3,000 ppm input feedwater and all tested compositions sampled at 3-5 points in time for both Fujifilm and Neosepta membranes.

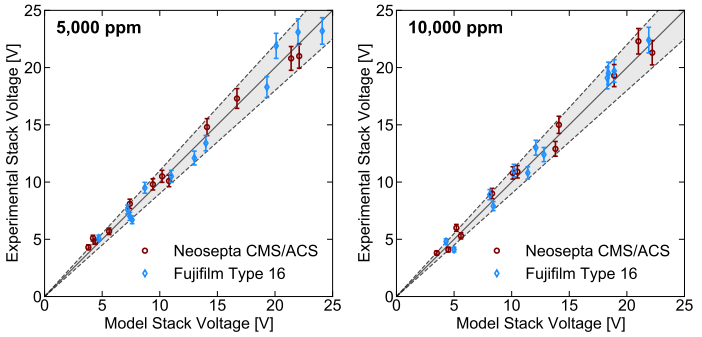

(c) Model predictions of stack voltage against experimental stack voltage for 5,000 ppm input feedwater and all tested compositions sampled at 3-5 points in time for both Fujifilm and Neosepta membranes.

(d) Model predictions of stack voltage against experimental stack voltage for 10,000 ppm input feedwater and all tested compositions sampled at 3-5 points in time for both Fujifilm and Neosepta membranes.

Figure 6: Model predictions of stack voltage against experimental stack voltage.

In Fig. 6(a) to 6(d) the shaded grey regions are the enveloping lines that represent a ±10% deviation between the model and experiments. For all salinities and compositions tested, all the points are seen to lie within the enveloping regions showing strong alignment between model predictions and the experiments.

At elevated salinities and compositions, the MSED stack is seen to operate at a lower stack voltage. Conversely, as the desalination process draws to a close, the stack voltage is seen to increase. Therefore, for a constant applied current density, the energy consumption of the stacks significantly increases. This rise creates a trade-off between obtaining lower levels of sodium desired in the diluate tank, and increasing energy consumption. Additional studies are currently being conducted to better characterize this trade-off.

3.4. Permselectivity predictions

The model is used to predict the permselectivity of different ion species throughout the MSED process. The results from the analysis and their comparisons to those obtained experimentally by Ahdab *et al.* are provided in Table 4 and 5 for the Neosepta and Fujifilm membranes, respectively [Ahdab et al., 2020a,b].

Table 4: Calcium, magnesium, and sodium permselectivities from the model and experiments for 13 brackish groundwater compositions using the Neosepta membranes. The first column indicates BGW composition and the relative uncertainties correspond to *t*-statistics for a 95% confidence limit. Comp. 4 (last row) corresponds to the experiments conducted by Ahdab *et al.* [Ahdab et al., 2020a] using the input water compositions from Cohen *et al.*'s study [Cohen et al., 2018] on MSED for agriculture.

TDS	P_{Na}^{Ca} (exp)	P_{Na}^{Ca} (mod)	P_{Na}^{Mg} (exp)	P_{Na}^{Mg} (mod)
1,542	0.27 ± 0.02	0.26 ± 0.02	0.15 ± 0.01	0.15 ± 0.02
2,687	0.23 ± 0.01	0.24 ± 0.02	0.13 ± 0.02	0.13 ± 0.02
4,190	0.28 ± 0.02	0.27 ± 0.01	0.14 ± 0.01	0.13 ± 0.02
10,810	0.26 ± 0.02	0.26 ± 0.02	0.13 ± 0.01	0.14 ± 0.01
1,380	0.25 ± 0.02	0.24 ± 0.01	0.10 ± 0.02	0.10 ± 0.01
3,013	0.22 ± 0.02	0.23 ± 0.01	0.11 ± 0.01	0.11 ± 0.02
4,643	0.20 ± 0.02	0.21 ± 0.02	0.11 ± 0.02	0.13 ± 0.02
10,660	0.27 ± 0.02	0.27 ± 0.01	0.18 ± 0.01	0.17 ± 0.02
1,391	0.29 ± 0.02	0.28 ± 0.01	0.20 ± 0.01	0.15 ± 0.01
2,813	0.27 ± 0.01	0.27 ± 0.02	0.16 ± 0.01	0.21 ± 0.01
4,668	0.29 ± 0.03	0.28 ± 0.01	0.14 ± 0.01	0.15 ± 0.02
10,771	0.24 ± 0.01	0.25 ± 0.01	0.17 ± 0.02	0.16 ± 0.01
2,588	0.27 ± 0.01	0.26 ± 0.01	0.16 ± 0.02	0.17 ± 0.01

Table 5: Calcium, magnesium, and sodium permselectivities from the model and experiments for 13 brackish groundwater compositions using the Fujifilm membranes. The relative uncertainties correspond to *t*-statistics for a 95% confidence limit.

TDS	P_{Na}^{Ca} (exp)	P_{Na}^{Ca} (mod)	P_{Na}^{Mg} (exp)	P_{Na}^{Mg} (mod)
1,295	0.21 ± 0.03	0.22 ± 0.02	0.09 ± 0.02	0.09 ± 0.02
2,858	0.14 ± 0.03	0.14 ± 0.02	0.06 ± 0.02	0.06 ± 0.01
4,408	0.19 ± 0.03	0.18 ± 0.01	0.09 ± 0.02	0.08 ± 0.02
10,396	0.16 ± 0.04	0.17 ± 0.03	0.09 ± 0.03	0.10 ± 0.02
1,483	0.18 ± 0.02	0.18 ± 0.01	0.05 ± 0.002	0.05 ± 0.01
2,895	0.10 ± 0.05	0.09 ± 0.04	0.06 ± 0.004	0.06 ± 0.005
4,756	0.19 ± 0.02	0.20 ± 0.02	0.10 ± 0.002	0.09 ± 0.004
7,814	0.22 ± 0.02	0.23 ± 0.01	0.09 ± 0.003	0.10 ± 0.004
1,450	0.13 ± 0.03	0.14 ± 0.01	0.07 ± 0.02	0.07 ± 0.01
2,683	0.22 ± 0.03	0.21 ± 0.02	0.10 ± 0.01	0.10 ± 0.01
4,276	0.22 ± 0.02	0.23 ± 0.01	0.05 ± 0.007	0.06 ± 0.01
8,491	0.21 ± 0.01	0.22 ± 0.02	0.09 ± 0.002	0.10 ± 0.008
2,564	0.20 ± 0.02	0.20 ± 0.01	0.08 ± 0.02	0.08 ± 0.01

Higher permselectivities are noted for calcium relative to magnesium (P_{Na}^{Ca} is greater than P_{Na}^{Mg}). The model predicts a permselectivity value of 0.15 ± 0.02 across all salinities and compositions for magnesium using the Neosepta membranes. For calcium, the model predicts 0.25 ± 0.02 across all salinities and compositions using the same set of membranes. These values correspond to ~7 sodium ions removed from the diluate stream for a given magnesium ion, and ~4 sodium ions removed from the diluate stream for every given calcium ion. Magnesium is expected to have better rejection rates due to its larger hydration energy (1904 kJ/mol) in comparison to that of calcium (1592 kJ/mol). This hydration energy corresponds to the size of the hydration shell that the ions need to shed prior to passing through the membranes. This phenomenon is observed in the results seen in Table 4. The model predictions are also seen to closely align with experimental data. Maximum errors obtained for the Neosepta membranes were on the order of 6% across all salinities and compositions.

Similarly for the Fujifilm membranes, the permselectivities are predicted by the model and compared to those determined experimentally by Ahdab *et al.* [Ahdab et al., 2020b]. The Fujifilm membranes demonstrate better selectivities in comparison to the Neosepta membranes based on both modelling and experimental studies. The model predictions for the magnesium permselectivity averaged 0.08 ± 0.01, while the calcium permselectivity averaged at 0.20 ± 0.01. The increased rejection of magnesium due to the larger hydration energies is still observed. The alignment between model and experiments for the Fujifilm membranes is about 8% across all salinities and compositions.

The permselectivity obtained across salinities and compositions were relatively consistent for both the model and experiments for each set of membranes. In the literature, any trends that are observed in transport numbers or selectivities are usually across large concentration ranges (all the way up to saturation). For the brackish water range, given the small range of salinities and composition considered, the lack of observable trends is expected [Ahdab et al., 2020a,b].

4. Implications for greenhouses

Using the models predictions for MSED permselectivity, fertilizer cost savings are investigated across the continental U.S. The USGS groundwater dataset provides access to 28,000 data points of full groundwater compositions data to within 5% of electroneutrality [Stanton et al., 2017]. The distribution of data points across the U.S. is provided in Appendix H. This section analyzes the efficacy of using MSED in treating brackish source water in comparison to the industry standard RO.

The primary contingents of fertilizer are macronutrients like calcium, magnesium, sulphates, phosphates, nitrates, and potassium. Water solubility is desirable to allow salts to dissociate in the water and get uptook by crops. Ubiquitously used salts for fertilizers include gypsum, epsom salt, potassium chloride and/or sulphate, ammonium nitrate and/or sodium nitrate, and ammonium phosphate. Each fertilizer provides different macronutrients in different proportions. Gypsum and epsom salt for example, are used in greenhouses to control the calcium and magnesium levels in the source water for irrigation. The addition of 3.06×10^{-4} kg of gypsum to 1 m^2 of soil results in a 110 ppm increase in calcium. Similarly, the addition of 4.09×10^{-4} kg of epsom to 1 m^2 of soil yields a 50 ppm increase in magnesium. Using available prices from Amazon, the average cost of elevating the concentration of a given ion by 1 ppm per m^2 of soil can be calculated [Amazon.com, Inc., b,a]. These values correspond to 2.69×10^{-3} \$ m^{-2} ppm^{-1} and 1.71×10^{-3} \$ m^{-2} ppm^{-1} for calcium and magnesium ions, respectively. Sulphates are added to the soil by blending other fertilizers to meet the required ratio; for the purposes of the work reported here, only calcium and magnesium savings are considered to determine a lower bound on the fertilizer savings when employing MSED.

Table 6: Water quality recommendations for agriculture [Yermiyahu et al., 2007, Will and Faust, 1999, Pick, 2011]. SAR values usually range from 0-7 Pick [2011], where sensitive crops should not be exposed to waters with SAR values above 4 Pick [2011]. For the potentially toxic ions: sodium, chloride, and boron, the toxicity limits are: 270 mg/L, 250 mg/L, and 1.8 mg/L, respectively Pick [2011].

Ion	Concentration (ppm)
Ca^{2+}	80-150
Mg^{2+}	30-50
Na^{+}	Low as possible
SO_4^{2-}	>50
Cl^{-}	>20

Based on irrigation water quality requirements (Table 6), source water that has calcium concentrations of above 150 ppm, magnesium concentrations of above 50 ppm, and sulphate concentrations of above 50 ppm can be defined as having treatment potential using MSED. Filtering the 28,000 samples in the USGS dataset to meet this requirement, 5069 samples remain (Fig. 7).

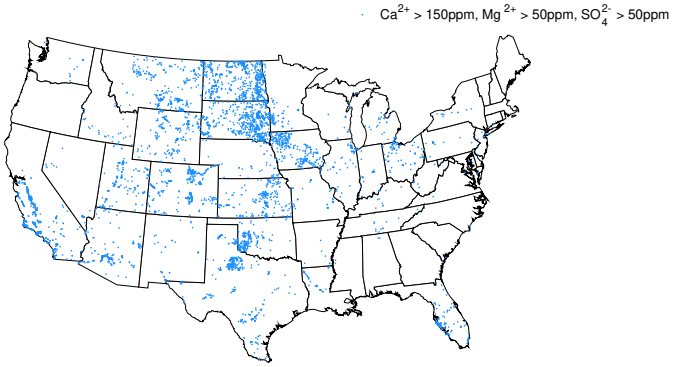

Figure 7: 5069 remaining samples in the USGS dataset that contain sufficient calcium, magnesium, and sulphate ions for treatment using MSED.

In the conducted analysis, the permselectivity of the Fujifilm membranes values obtained from the model in Section 3.4 are used in characterizing fertilizer savings. Previous work conducted by Ahdab *et al.* showed a marginal increase in cost savings when employing the Fujifilm membranes over the Neosepta membranes. The increase in savings was on the order of 1% using average permselectivity obtained from experiments [Ahdab et al., 2020b]. For the Fujifilm membranes, the average permselectivities for calcium and magnesium are $P_{Na}^{Ca} = 0.20$ and $P_{Na}^{Mg} = 0.08$, respectively.

By setting the dominant ion, calcium, to be equal to that of the water quality requirements, the permselectivity obtained from the

model can be used to calculate the final sodium and magnesium concentrations present in the product water. Since RO is used as a comparison point for fertilizer cost savings, the difference in ion percentage reductions between MSED and RO is used in all calculations. Ion percentage reductions seen by RO are summarized in Table 7.

Eq. (33) calculates the ion percentage savings from employing MSED relative to RO. These percentage savings can be converted into ppm savings using Eq. (34), which can subsequently be extended into a fertilizer cost saving value calculated by Eq. (35). In all conducted studies, the sodium concentration was always below 100 ppm.

$$\mathrm{Sav}_{\%,\mathrm{div}} = \left[\left(\frac{C_{\mathrm{div},i} - C_{\mathrm{div},f|\mathrm{RO}}}{C_{\mathrm{div},i}}\right) - \left(\frac{C_{\mathrm{div},i} - C_{\mathrm{div},f|\mathrm{MSED}}}{C_{\mathrm{div},i}}\right)\right] \times 100\% \tag{33}$$

$$\mathrm{Sav}_{\mathrm{ppm,div}} = 0.01(C_{\mathrm{div},i}\mathrm{Sav}_{\%,\mathrm{div}}) \tag{34}$$

$$\mathrm{Sav}_{\$,\mathrm{div}} = \mathrm{Sav}_{\mathrm{ppm,div}}\mathrm{Fer}_{\$,\mathrm{div}} \tag{35}$$

Using this framework and the average selectivities from the model,

Table 7: Percentage reductions of relevant ion species using RO: $\left[\left(\frac{C_{\mathrm{div},i}-C_{\mathrm{div},f|\mathrm{RO}}}{C_{\mathrm{div},i}}\right)-\left(\frac{C_{\mathrm{div},i}-C_{\mathrm{div},f|\mathrm{MSED}}}{C_{\mathrm{div},i}}\right)\right]\times 100\%$ [Ahdab et al., 2020a].

Ion	Ion reduction (%)
Ca^{2+}	90
Mg^{2+}	99
Na^{+}	97
SO_4^{2-}	99
Cl^{-}	98

$\mathrm{Sav}_{\%,\mathrm{Ca}}$ and $\mathrm{Sav}_{\%,\mathrm{Mg}}$ values of 80 and 92 are calculated, respectively. These values correspond to $\mathrm{Sav}_{\mathrm{ppm,Ca}}$ and $\mathrm{Sav}_{\mathrm{ppm,Mg}}$ values of 135 and 81, respectively. The ppm savings are converted into cost values that show an average saving of $4,991 per hectare for greenhouses if MSED is employed as a desalination technology instead of RO. By varying the model permselectivity to within their standard deviations, the range of savings is observed between 4,940 and 5,080 $/ha.

The cost savings, when extended to the various input groundwater compositions, yield the geographic savings distribution seen in Fig. 8. The illustrated savings are a result of reduced fertilizer consumption, but do not take into account the difference in capital and operating costs between MSED and RO Ahdab et al. [2020a,b]. Regions with a high density of data points align with areas of high agricultural activity and greenhouse infrastructure [Rehman et al., 20-24 Oct. 2019, Dubai, U.A.E, Ahdab et al., 2020a,b]. As the fertilizer savings increase linearly with the size of greenhouses, and the CapEx and OpEx exploit economies of scale for larger greenhouses, significant savings can be expected through MSED adoption across the U.S. In addition, MSED as a technology operates at higher recovery ratios than RO at these salinities and compositions, suggesting even more savings from more efficient water use. Additional studies are currently under way to investigate the optimal techno-economic performance of these systems for greenhouses.

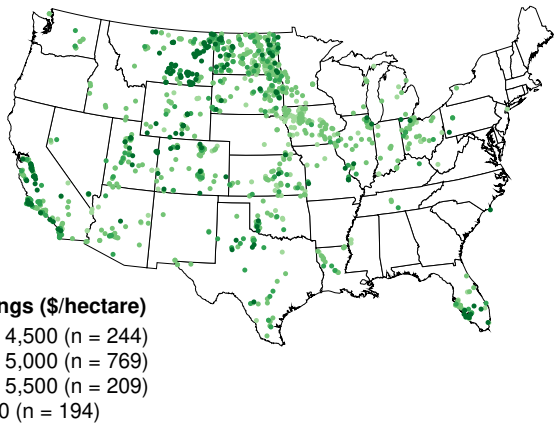

Figure 8: Map of fertilizer savings using MSED with Fujifilm's membranes across the continental U.S.

5. Conclusion

A computational model for MSED is proposed by extending conventional ED modelling techniques. The model is validated against 26 experiments to within uncertainties of 6% and 8% for the Neosepta and Fujifilm membranes, respectively. The model is used to predict transport numbers and permeabilities of individual cations and anions within the incoming source water throughout the desalination process. These transport numbers are used to predict permselectivities for a given set of membranes and incoming source water. The voltage across the MSED stack is also matched to within 10% for all experiments conducted. The permselectivities are used in conjunction with available groundwater data from USGS to predict fertilizer savings when employing MSED as a technology for greenhouse irrigation across the US. Savings of $4,991 per hectare are obtained on average through the conducted study. These values, in addition to expected water savings from using MSED relative to RO suggest the potential for using MSED for greenhouses.

6. Acknowledgements

The authors would like to thank the National Science Foundation and the Bureau of Reclamation under Agreement Number R17AC00135 for funding the research reported in this paper. Additional support was provided by the Centers for Mechanical Engineering Research and Education at MIT and SUSTech (MechERE Centers at MIT and SUSTech).

Appendix A. Derivation of the flux equations from the complete Nernst-Planck partial differential equations

The complete Nernst-Planck equations [Probstein, 2005] of transport can be written for a given cation and anion by Eq. (A.1) and Eq. (A.2), respectively as follows:

$$J_c = -D_c \nabla C_c - \frac{D_c z_c \mathscr{F}}{RT} C_c \nabla \Phi \tag{A.1}$$

$$J_a = -D_a \nabla C_a - \frac{D_a z_a \mathscr{F}}{RT} C_a \nabla \Phi \tag{A.2}$$

where D is the diffusion coefficient, C is the concentration, z is the valence, $\mathscr{F}$ is Faraday's constant, R is the universal gas constant, and T is the temperature. c and a denote the cation and anion pair, respectively. The two equations can be rearranged and summed to provide the following expression:

$$-\frac{J_c}{D_c} - \frac{J_a}{D_a} = \nabla C_c + \nabla C_a + \frac{\mathscr{F}}{RT} \nabla \Phi \cancelto{0}{(z_c C_c + z_a C_a)} \tag{A.3}$$

where the electroneutrality condition leads to the migration terms in the sum going to zero. Thus:

$$-\frac{J_c}{D_c} - \frac{J_a}{D_a} = \nabla C_c + \nabla C_a \tag{A.4}$$

In electrochemical transport, the applied current density can be rewritten as a sum of the individual ion fluxes in the solution, $i = \mathscr{F} \sum_k z_k J_k$. Expanding this summation for a given anion and cation pairing provides:

$$i = \mathscr{F} (z_a J_a + z_c J_c) \tag{A.5}$$

Rearranging the above equation to be an explicit function of the anion flux yields:

$$J_a = \frac{i}{z_a \mathscr{F}} - \frac{z_c}{z_a} J_c \tag{A.6}$$

Assuming a given salt dissociates entirely in solution, an expression can be established between the valence of the cation-anion pair and the stoichiometric coefficients seen below:

$$z_a \nu_a + z_c \nu_c = 0 \implies \frac{z_a}{z_c} = -\frac{\nu_c}{\nu_a} \tag{A.7}$$

where ν is the stoichiometric coefficient. Using this equation, all instances of the cation and anion valence can be substituted by stoichiometric coefficients. Similarly, a relation between the total concentration and the concentration of each ion species can be obtained using stoichiometric coefficients, where, $\nu_c C = C_c$ and $\nu_a C = C_a$. Using these two relations, Eq. (A.4) can be rewritten in the following form:

$$J_c \left[\frac{1}{D_c} + \left(\frac{\nu_a}{\nu_c} \right) \frac{1}{D_a} \right] = -\frac{i}{D_a z_a \mathscr{F}} - (\nu_c + \nu_a) \nabla C \tag{A.8}$$

Rearranging the equation to isolate for the cation flux, Eq. (A.9) is obtained:

$$J_c = \left[\frac{D_c}{D_a - (z_c/z_a) D_c} \right] \left(\frac{i}{z_a \mathscr{F}} \right) - (\nu_c + \nu_a) \left[\frac{D_c D_a}{D_a - (z_c/z_a) D_c} \right] \tag{A.9}$$

In this form, transport numbers are introduced. In the limit of negligible concentration gradients, it can be formulated as follows:

$$T_c = \frac{z_c^2 D_c C_c}{\sum_k z_k^2 D_k C_k} = \frac{z_c^2 D_c C_c}{z_a^2 D_a C_a + z_c^2 D_c C_c} \tag{A.10}$$

where T_c is the transport number of the cation. The transport numbers in the main text are all fitted directly from experimental data using Eq. (A.14) and Eq. (A.15) and do not neglect concentration gradients. T_c can be reduced to:

$$T_c = \frac{z_c D_c}{z_c D_c - z_a D_a} \tag{A.11}$$

In addition to this model, the Nernst-Hartley equation can be used to formulate a relation between the salt diffusion coefficient and the ion-specific diffusion coefficients as a function of the stoichiometric coefficients [Clunie et al., 1992]:

$$D_{\text{salt}} = \frac{(\nu_a + \nu_c) D_a D_c}{\nu_a D_c + \nu_c D_a} \tag{A.12}$$

Substituting Eq. (A.11) and Eq. (A.12) into Eq. (A.9), the penultimate form of the cation flux equation is:

$$J_c = \frac{T_c i}{z_c \mathscr{F}} - D_{\text{salt}} \nabla C_c \tag{A.13}$$

For practical purposes, $D_c \nabla C_c$ can be rewritten using permeabilities instead of diffusion coefficients, given their ease of measurement. This leads to the final form of the Nernst-Planck equations used for modelling ion and water transport in the MSED model:

$$J_c = \frac{T_c i}{z_c \mathscr{F}} - L_c \Delta C_c \tag{A.14}$$

The anion species are described by a similar equation:

$$J_a = \frac{T_a i}{z_a \mathscr{F}} - L_a \Delta C_a \tag{A.15}$$

Although these equations correspond to cation and anion fluxes for binary systems, the ion fluxes are superimposed to account for all ion species in the solution. Similar approaches have been observed for high salinity solutions, as seen in Koter and Warszawski. Therefore, at the low concentrations that the model is optimized for, errors are expected to be negligible Koter and Warszawski [2006].

Appendix B. Ion species and water balances in the MSED stack

The governing transport equations for the MSED stack are as follows:

$$\frac{dQ_d}{dA_m} = -\frac{dQ_c}{dA_m} = -N_{cp} J_w(x) \tag{B.1}$$

$$\frac{d(C_{j,d} Q_d)}{dA_m} = -\frac{d(C_{j,c} Q_c)}{dA_m} = -N_{cp} J_j(x) \tag{B.2}$$

where Q is the flow rate, A_m is the membrane area, N_{cp} is the number of cell pairs, C is the concentration, and J is the flux. The subscripts c, d, j, and w denote the concentrate, diluate, chemical species, and

water, respectively. Expanding out Eq. (B.2) using the product rule yields:

$$\frac{d(C_{j,d}Q_d)}{dA_m} = Q_d(x)\frac{dC_{j,d}}{dA_m} + C_{j,d}(x)\frac{dQ_d}{dA_m} \tag{B.3}$$

In the second term of the equation on the right hand side, Eq. (B.1) can be substituted into it to yield:

$$\frac{d(C_{j,d}Q_d)}{dA_m} = Q_d(x)\frac{dC_{j,d}}{dA_m} - N_{cp}J_w(x) = -N_{cp}J_j(x) \tag{B.4}$$

Rearranging Eq. (B.4) to make it an explicit function of the concentration gradient provides:

$$\frac{dC_{j,d}}{dA_m} = \frac{1}{Q_d(x)}\left[N_{cp}J_w(x) - N_{cp}J_j(x)\right] \tag{B.5}$$

Here, the membrane area can be distributed into: $dA_m = hdx$ due to the constant, spatially-invariant channel height. This is substituted into the left-hand side. In addition, N_{cp} can be factorized out of the brackets to give the final concentration gradient expression:

$$\frac{dC_{j,d}}{dx} = \frac{hN_{cp}}{Q_d(x)}\left[C_{j,d}(x)J_w(x) - J_j(x)\right] \tag{B.6}$$

Similarly, for the concentrate stream, a corresponding expression can be calculated:

$$\frac{dC_{j,c}}{dx} = -\frac{hN_{cp}}{Q_c(x)}\left[C_{j,c}(x)J_w(x) - J_j(x)\right] \tag{B.7}$$

Appendix C. Grid independence studies

A grid independence study is performed on the one-dimensional transport model to find a balance between numerical accuracy and computational cost. The relative percentage error in the concentration of all present ion species at the exit of the stack is plotted as a function of the total number of nodes used to discretize the MSED stack. Fig. C.1 presents the results for an average diluate bulk velocity of v_{dil} = 3 cm/s and v_{dil} = 10 cm/s. The lower value represents a lower bound for the feedwater flow speed used in all conducted experimental tests, while the higher value represents the maximum flow speed seen by the stack in all conducted studies reported in this work. The initial operating flow velocity for all performed tests was 5.6 cm/s.

The final number of nodes selected was 150. The percentage error in the normalized outlet concentration of all ion species for the most adverse conditions expected in the stack has stabilized beyond this point.

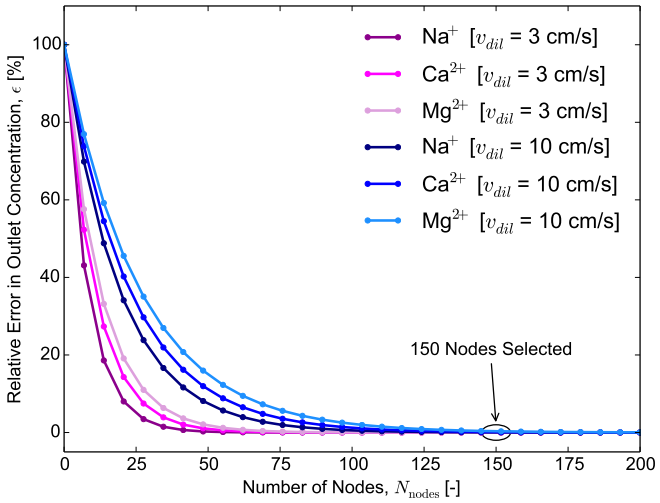

Figure C.1: Normalized percentage error in concentration of each ion species at the outlet of the stack as a function of the number of discrete nodes in the MSED stack. A total node count of 150 was selected for all model results reported in this work.

Appendix D. Experimental setup

The batch MSED experiment flow diagram is seen in Fig. D.1. This setup has been previously characterized by Ahdab *et al.* and is used for additional model validation studies conducted in this work [Ahdab et al., 2020a,b]. The experimental setup employs a PCCell ED200 stack retrofitted with 10 cell pairs of ion exchange membranes. Two sets of membranes are tested in this work: 1) Monovalent selective CMS/ACS Neosepta membranes and 2) Monovalent selective Fujifilm Type 16 membranes. The total active membrane area of the MSED stack is A_m = 0.43 m^2. The setup also includes 20 spacers of 0.5 mm thickness and two end spacers in the electrode streams each of 1 mm thickness.

The stack is comprised of three circuit loops: the diluate loop, the concentrate loop, and the electrode rinse loop. The diluate, concentrate, and electrode rinse tanks have the following volumes: 1 L, 4 L, and 4 L, respectively. This effectively sets the system recovery ratio for a full batch cycle at ~20%. Feedwaters are simulated that consisted of different compositions of sodium, calcium, magnesium, chloride, and sulphates. Deionized water is used in conjunction with the following salts to create the feedwater: NaCl, Na_2SO_4, $CaCl_2$, $CaSO_4$, $MgCl_2$, and $MgSO_4$. This simulated groundwater serves as an input into the diluate and concentrate tanks. Sodium sulphate solution of 0.2 M is used as an electrode rinse. Centrifugal pumps (Iwaki, model MD-55R 135 (T)) circulate the three streams, and valved-rotameters regulate the constant flow rate of 95 LPH.

The flow channel height in the stack is 0.5 mm. The power supply (GW-INSTEK GPR-60600) applies a potential difference across the stack to induce ion transport and separation. Feed and product water composition are collected and measured using an inductively coupled plasma optical emission spectrometer (ICP-OES) at different stages of the experiment in both the diluate and concentrate streams. A heat exchanger regulates the concentrate temperature. Subsequently, the stack effectively serves as a second heat exchanger that regulates the diluate temperature. All tests are conducted at 25°C. The membranes are prepared by taking a 1 m^2 sheet of Neosepta and Fujifilm membranes and cutting them into individual membranes with 207 cm^2 of active area in accordance with the PCCell ED200 stack requirements. The membranes were stored in water when not in use to prevent dry out.

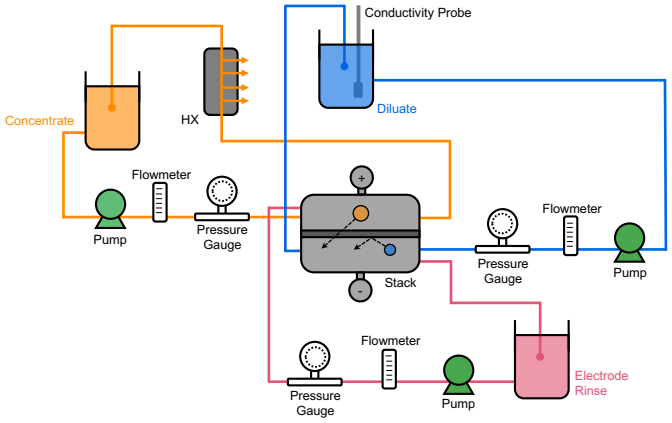

Figure D.1: Batch MSED system diagram (from studies conducted by Rehman *et al.* and Ahdab *et al.* [Rehman et al., 20-24 Oct. 2019, Dubai, U.A.E, Ahdab et al., 2020a]). 3 circulation loops present: diluate circuit (blue), concentrate circuit (orange), and electrode rinse circuit (pink).

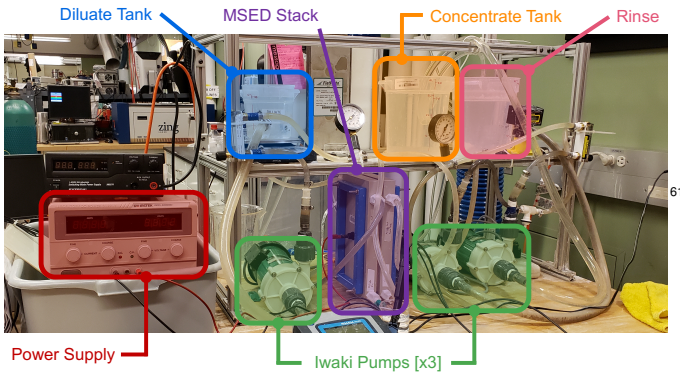

Figure D.2: Batch MSED experimental setup (based on studies conducted by Rehman *et al.* and Ahdab *et al.* [Rehman et al., 20-24 Oct. 2019, Dubai, U.A.E, Ahdab et al., 2020a]).

Appendix E. Membrane resistance studies and curve fits

Membrane resistance for both cation and anion exchange membranes vary as a function of salinity. Based on experiments conducted by Ahdab *et al.* [Ahdab et al., 2020a], curves were fit to the data (as seen in Fig. E.1). These curves serves as inputs for the model in determining the stack resistance. The increasing resistance at low concentrations is typical of ion exchange membranes and one of the potential drawbacks of using ED or MSED for solutions of low salinity.

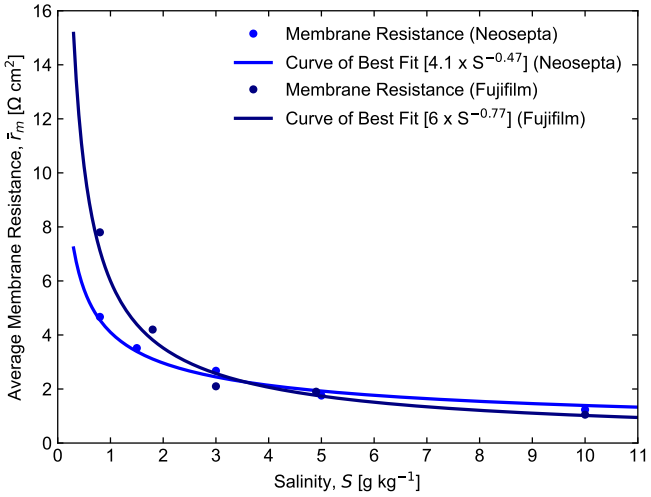

Figure E.1: Average membrane resistance as a function of salinity. Best fit lines included for both Neosepta [Ahdab et al., 2020a] and Fujifilm membranes [Ahdab et al., 2020b]: $\bar{r}_{m,\text{Neosepta}} = 4.1 \times S^{-0.47}$ and $\bar{r}_{m,\text{Fujifilm}} = 6.0 \times S^{-0.77}$, respectively.

Appendix F. Molar conductivity of all electrolytes

The molar conductivity of the studied salts is plotted as a function of concentration in Fig. F.1. Exponential curves were fit to the data and interpolated at each location across the MSED stack to determine the molar conductivity of the solution.

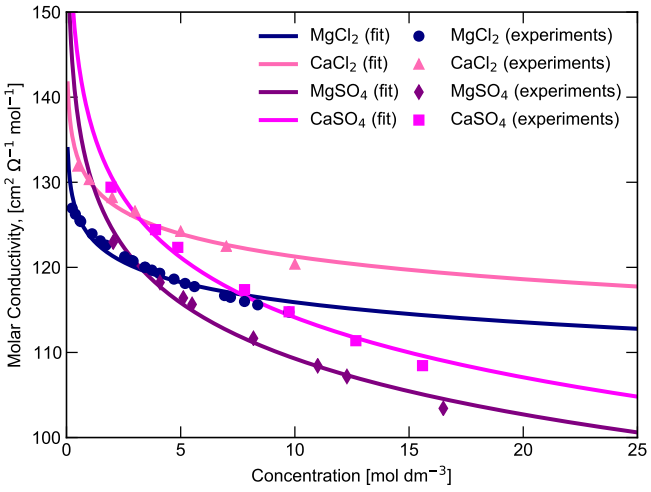

Figure F.1: Molar conductivity as a function of concentration for NaCl, $CaCl_2$, $MgCl_2$, $CaSO_4$, and $MgSO_4$. Data obtained from multiple sources [Wright et al., 2018b, Benson and Gordon, 1945, Bianchi et al., 1988, Hsieh et al., 1982].

Appendix G. Pitzer-Kim model validation and table of parameters

For the Pitzer-Kim model, the second and third virial coefficients are expressed as:

$$B^{\phi}_{MX} = \beta^{(0)}_{MX} + \beta^{(1)}_{MX} e^{-\alpha_{MX}\sqrt{I}} + \beta^{(2)}_{MX} e^{-12\sqrt{I}} \tag{G.1}$$

$$B_{MX} = \beta^{(0)}_{MX} + \beta^{(1)}_{MX} g(\alpha_{MX}\sqrt{I}) + \beta^{(2)}_{MX} g(12\sqrt{I}) \tag{G.2}$$

$$B'_{MX} = \beta^{(1)}_{MX} \frac{g'(\alpha_{MX}\sqrt{I})}{I} + \beta^{(2)}_{MX} \frac{g'(12\sqrt{I})}{I} \tag{G.3}$$

$$C_{MX} = \frac{C^{\phi}_{MX}}{2|z_M z_X|^{0.5}} \tag{G.4}$$

where I is $\frac{1}{2}\sum_i b_i z_i^2$, and Z is $\sum_i b_i |z_i|$. Values for the Pitzer-Kim model: $\beta^{(0)}_{MX}$, $\beta^{(1)}_{MX}$, $\beta^{(2)}_{MX}$, and C^{ϕ}_{MX} are fixed for a given ion pairing and are provided in Table G.1.

Table G.1: Relevant binary parameters for all salts reported in this work [Harvie and Weare, 1980].

Salt	$\beta^{(0)}_{MX}$	$\beta^{(1)}_{MX}$	$\beta^{(2)}_{MX}$	C^{ϕ}_{MX}
NaCl	0.0765	0.2664	0	0.00127
Na_2SO_4	0.0196	1.113	0	0.00497
$CaCl_2$	0.3159	1.614	0	−0.00034
$CaSO_4$	0.2000	2.650	−54.24	0.01000
$MgCl_2$	0.3524	1.682	0	0.00519
$MgSO_4$	0.2210	3.343	−37.23	0.02500

For 2-2 electrolytes and higher non-univalent pairs, $\alpha_{MX} = 1.4$. For all other simpler pairing (1-1, 1-2, 2-1), α_{MX} is usually 2. Similarly, for 2-2 electrolytes and other high valence pairs, $\beta^{(2)}_{MX}$ is non-zero. $\beta^{(2)}_{MX} = 0$ for univalent pairs and other simple ionic pairing (1-2, 2-1). The functions $g(\xi)$ and $g'(\xi)$ are provided below in Eq. (G.5) and Eq. (G.6):

$$g(\xi) = \left(\frac{2}{\xi^2}\right)\left(1 - (1+\xi)e^{-\xi}\right) \tag{G.5}$$

$$g'(\xi) = -\left(\frac{2}{\xi^2}\right)\left(1 - \left(1 + \xi + \frac{\xi^2}{2}\right)e^{-\xi}\right) \tag{G.6}$$

where ξ is a function of ionic strength and can take on the values $\alpha_{MX}\sqrt{I}$ and/or $12\sqrt{I}$. The second virial coefficient, Φ is a function of ionic strength. The different forms of Φ required are seen below.

$$\Phi^{\phi}_{ij} = \theta_{ij} + {}^{E}\theta_{ij}(I) + I\,{}^{E}\theta'_{ij}(I) \tag{G.7}$$

$$\Phi_{ij} = \theta_{ij} + {}^{E}\theta'_{ij}(I) \tag{G.8}$$

$$\Phi'_{ij} = {}^{E}\theta_{ij}(I) \tag{G.9}$$

Here, θ_{ij} is a function of the electrolyte pair. Functions ${}^{E}\theta_{ij}(I)$ and ${}^{E}\theta'_{ij}(I)$ depend on the ionic strength of the solution and the particular ionic pair. The complete form of these functions and the integrals used to evaluate them are provided by Eq. (G.10) to Eq. (G.13).

$${}^{E}\theta_{ij}(I) = \frac{z_i z_j}{4I}\left(J_0(x_{ij}) - \frac{1}{2}J_0(x_{ii}) - \frac{1}{2}J_0(x_{jj})\right) \tag{G.10}$$

$${}^{E}\theta'_{ij}(I) = \frac{z_i z_j}{8I^2}\left(J_1(x_{ij}) - \frac{1}{2}J_1(x_{ii}) - \frac{1}{2}J_1(x_{jj})\right) - \frac{{}^{E}\theta_{ij}(I)}{I} \tag{G.11}$$

Here, the pertinent integrals are:

$$J_0(\nu) = \frac{1}{4}\nu - 1 + \frac{1}{\nu}\int_0^{\infty}\left[1 - e^{-\frac{\nu}{\mu}e^{-\mu}}\right]\mu^2 d\mu \tag{G.12}$$

$$J_1(\nu) = \frac{1}{4}\nu - 1 + \frac{1}{\nu}\int_0^{\infty}\left[1 - \left(1 + \frac{\nu}{\mu}e^{-\mu}\right)e^{-\frac{\nu}{\mu}e^{-\mu}}\right]\mu^2 d\mu \tag{G.13}$$

Lastly, reference chemical potential data was required to calculate Donnan potentials. The data for the pertinent ions can be found in Table G.2 below.

Table G.2: Dimensionless standard reference state chemical potential data for relevant ion species in the MSED model [Harvie and Weare, 1980].

Ion Species	μ°_j/RT
Na^+	−105.65
Ca^{2+}	−223.30
Mg^{2+}	−183.47
Cl^-	−52.96
SO_4^{2-}	−300.39

Appendix H. USGS groundwater dataset

A 2017 national assessment of source water across the continental US serves as the primary source of information regarding the national water distribution. The assessment was performed by USGS and the study includes a major-ions dataset with over 100,000 groundwater wells and a dissolved solids dataset with over 300,000 groundwater wells in the U.S. and four of its territories. We use U.S. continental data from the USGS major-ions dataset. It contains complete composition data for 28,000 samples in the brackish water range across the U.S. (Fig. H.1).

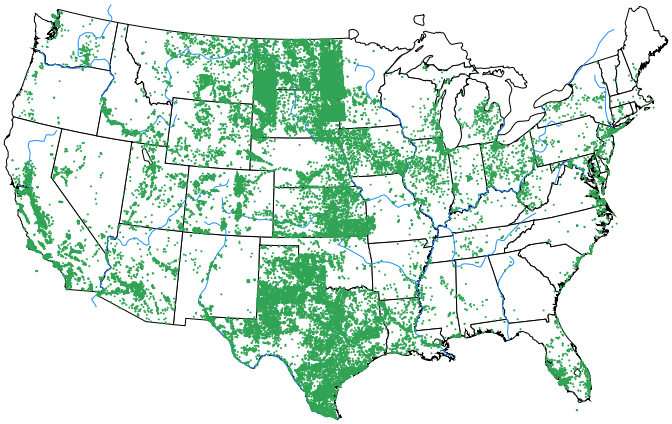

Figure H.1: The distribution of full groundwater composition data to within 5% of electroneutrality from 28,000 BGW samples in the USGS major-ions dataset.

References

Y. D. Ahdab, D. Rehman, and J. H. Lienhard. Brackish water desalination for greenhouses: improving groundwater quality for irrigation using monovalent selective electrodialysis reversal. *Journal of Membrane Science*, page 118072, 2020a. URL https://doi.org/10.1016/j.memsci.2020.118072.

Y. D. Ahdab, D. Rehman, G. Schücking, M. Barbosa, and J. H. Lienhard. Treating irrigation water using high-performance membranes for monovalent selective electrodialysis. *ACS ES&T Water*, 2020b. doi: 10.1021/acsestwater.0c00012. URL https://doi.org/10.1021/acsestwater.0c00012.

Y. D. Ahdab, G. Schücking, D. Rehman, and J. H. Lienhard. Treatment of greenhouse wastewater for reuse or disposal using monovalent selective electrodialysis. *Desalination*, 507:115037, 2021. ISSN 0011-9164. URL https://doi.org/10.1016/j.desal.2021.115037.

Amazon.com, Inc. Product: Epsoak Epsom Salt - 5 lbs. Magnesium Sulfate USP, a. URL https://www.amazon.com/Epsoak-Epsom-Salt-Magnesium-Sulfate/dp/B004N79BYC.

Amazon.com, Inc. Product: Calcium Sulfate Dihydrate - Gypsum - 5 Pounds, b. URL https://www.amazon.com/Calcium-Sulfate-Dihydrate-Gypsum-CaSO42H2O/dp/B008LEV0V0.

G. C. Benson and A. R. Gordon. The conductance of aqueous solutions of Calcium Chloride at temperatures from 15° to 45°C. *The Journal of Chemical Physics*, 13(11):470–472, 1945. URL https://doi.org/10.1063/1.1723980.

H. Bianchi, H. R. Corti, and R. Fernandez-Prini. The conductivity of dilute aqueous solutions of magnesium chloride at 25 °C. *Journal of Solution Chemistry*, 17(11):1059–1065, 1988. URL https://doi.org/10.1007/BF00647801.

S. C. Chapra and R. P. Canale. *Numerical Methods for Engineers*. McGraw-Hill Higher Education, Boston, Massachusetts, 6th edition, 2010. ISBN 978-0-07-340106-5.

K. M. Chehayeb, D. M. Farhat, K. G. Nayar, and J. H. Lienhard. Optimal design and operation of electrodialysis for brackish-water desalination and for high-salinity brine concentration. *Desalination*, 420:167–182, 2017. URL https://doi.org/10.1016/j.desal.2017.07.003.

J. C. Clunie, N. L. Burns, and J. K. Baird. Nernst-hartley evaluation of the interdiffusion coefficient of aqueous nickel sulfamate using new measurements of the equivalent conductances of the ions. *Journal of Electroanalytical Chemistry*, 328(1):317 – 320, 1992. doi: https://doi.org/10.1016/0022-0728(92)80188-A. URL http://www.sciencedirect.com/science/article/pii/002207289280188A. An International Journal Devoted to All Aspects of Electrode Kinetics, Interfacial Structure, Properties of Electrolytes, Colloid and Biological Electrochemistry.

B. Cohen, N. Lazarovitch, and J. Gilron. Upgrading groundwater for irrigation using monovalent selective electrodialysis. *Desalination*, 431:126–139, 2018. URL https://doi.org/10.1016/j.desal.2017.10.030.

M. Fidaleo and M. Moresi. Optimal strategy to model the electrodialytic recovery of a strong electrolyte. *Journal of Membrane Science*, 260(1):90 – 111, 2005. doi: https://doi.org/10.1016/j.memsci.2005.01.048. URL http://www.sciencedirect.com/science/article/pii/S0376738805002486.

C. E. Harvie and J. H. Weare. The prediction of mineral solubilities in natural waters: the Na-K-Mg-Ca-Cl-SO_4-H_2O system from zero to high concentration at 25 °C. *Geochimica et Cosmochimica Acta*, 44(7):981–997, 1980. URL https://doi.org/10.1016/0016-7037(84)90098-X.

A.-K. Hsieh, K.-P. Ang, and M. Chang. Conductance of calcium sulphate and magnesium sulphate in aqueous solution at high pressure. *J. Chem. Soc., Faraday Trans. 1*, 78:2455–2466, 1982. URL http://dx.doi.org/10.1039/F19827802455.

W. Jiang, L. Lin, X. Xu, H. Wang, and P. Xu. Physicochemical and electrochemical characterization of cation-exchange membranes modified with polyethyleneimine for elucidating enhanced monovalent permselectivity of electrodialysis. *Journal of Membrane Science*, 572:545–556, 2019. URL https://doi.org/10.1016/j.memsci.2018.11.038.

H. Kawate, K. Miyaso, and M. Takiguchi. Energy savings in salt manufacture by ion exchange membrane electrodialysis. In *Sixth International Symposium on Salt*, volume 2, pages 471–479, 1983.

G. Kortüm. Treatise on Electrochemistry. Technical report, Elsevier, 1965. URL https://doi.org/10.1021/ed043pA666.1.

S. Koter and A. Warszawski. A new model for characterization of bipolar membrane electrodialysis of brine. *Desalination*, 198(1):111–123, 2006. ISSN 0011-9164. URL https://doi.org/10.1016/j.desal.2006.09.016. The Second Membrane Science and Technology Conference of Visegrad Countries (PERMEA 2005).

O. Kuroda, S. Takahashi, and M. Nomura. Characteristics of flow and mass transfer rate in an electrodialyzer compartment including spacer. *Desalination*, 46(1-3):225–232, 1983. URL https://doi.org/10.1016/0011-9164(83)87159-8.

T. Luo, S. Abdu, and M. Wessling. Selectivity of ion exchange membranes: A review. *Journal of Membrane Science*, 555:429–454, 2018. URL https://doi.org/10.1016/j.memsci.2018.03.051.

R. K. McGovern, A. M. Weiner, L. Sun, C. G. Chambers, S. M. Zubair, and J. H. Lienhard. On the cost of electrodialysis for the desalination of high salinity feeds. *Applied Energy*, 136:649–661, 2014. URL https://doi.org/10.1016/j.apenergy.2014.09.050.

K. G. Nayar, M. H. Sharqawy, L. D. Banchik, and J. H. Lienhard. Thermophysical properties of seawater: A review and new correlations that include pressure dependence. *Desalination*, 390:1–24, 2016. URL https://doi.org/10.1016/j.desal.2016.02.024.

J. M. Ortiz, J. A. Sotoca, E. Expósito, F. Gallud, V. García-García, V. Montiel, and A. Aldaz. Brackish water desalination by electrodialysis: batch recirculation operation modeling. *Journal of Membrane Science*, 252(1):65 – 75, 2005. URL https://doi.org/10.1016/j.memsci.2004.11.021.

T. Pick. Assessing water quality for human consumption, agriculture, and aquatic life uses. *Environment Technical Note MT-1 (Rev2), Natural Resources Conservation Service*, 2011. URL https://www.nrcs.usda.gov/Internet/FSE_DOCUMENTS/nrcs144p2_051302.pdf.

K. S. Pitzer. Thermodynamics of electrolytes. I. Theoretical basis and general equations. *The Journal of Physical Chemistry*, 77(2):268–277, 1973. URL https://doi.org/10.1021/j100621a026.

K. S. Pitzer. Thermodynamics of electrolytes. V. Effects of higher-order electrostatic terms. *Journal of Solution Chemistry*, 4(3):249–265, 1975. URL https://doi.org/10.1007/BF00646562.

K. S. Pitzer and J. J. Kim. Thermodynamics of electrolytes. IV. Activity and osmotic coefficients for mixed electrolytes. *Journal of the American Chemical Society*, 96(18):5701–5707, 1974. URL https://doi.org/10.1021/ja00825a004.

K. S. Pitzer and G. Mayorga. Thermodynamics of electrolytes. II. Activity and osmotic coefficients for strong electrolytes with one or both ions univalent. *The Journal of Physical Chemistry*, 77(19):2300–2308, 1973. URL https://doi.org/10.1021/j100638a009.

K. S. Pitzer and G. Mayorga. Thermodynamics of electrolytes. III. Activity and osmotic coefficients for 2–2 electrolytes. *Journal of Solution Chemistry*, 3 (7):539–546, 1974. URL https://doi.org/10.1007/BF00648138.

R. F. Probstein. *Physicochemical Hydrodynamics: An Introduction*. Wiley, 2005. ISBN 9780471725121. URL https://books.google.ca/books?id=Drm_YDcuv0MC.

D. Rehman. Monovalent selective electrodialysis: optimizing energetics for desalination and mineral recovery. 15 May 2020. URL https://hdl.handle.net/1721.1/127122. Massachusetts Institute of Technology (MIT); Master's (S.M.) Thesis.

D. Rehman, Y. D. Ahdab, and J. H. Lienhard. Improving groundwater quality for irrigation using monovalent selective electrodialysis. 20-24 Oct. 2019, Dubai, U.A.E. URL https://hdl.handle.net/1721.1/124385. IDA Ref. No. IDAWC19-Rehman.

M. Reig, X. Vecino, C. Valderrama, O. Gibert, and J.-L. Cortina. Application of selectrodialysis for the removal of as from metallurgical process waters: Recovery of Cu and Zn. *Separation and Purification Technology*, 195:404–412, 2018. URL https://doi.org/10.1016/j.seppur.2017.12.040.

G. Saracco. Transport properties of monovalent-ion-permselective membranes. *Chemical Engineering Science*, 52(17):3019–3031, 1997. URL https://doi.org/10.1016/S0009-2509(97)00107-3.

G. Saracco and M. C. Zanetti. Ion transport through monovalent-anion-permselective membranes. *Industrial & Engineering Chemistry Research*, 33(1):96–101, 1994. URL https://doi.org/10.1021/ie00025a013.

H. Sato, M. Yui, and H. Yoshikawa. Ionic diffusion coefficients of Cs^+, Pb^{2+}, Sm^{3+}, Ni^{2+}, SeO_4^{2-} and TcO_4^- in free water determined from conductivity measurements. *Journal of Nuclear Science and Technology*, 33(12): 950–955, 1996. URL https://doi.org/10.1080/18811248.1996.9732037.

S. R. Shah, N. C. Wright, P. A. Nepsky, and A. G. Winter. Cost-optimal design of a batch electrodialysis system for domestic desalination of brackish

groundwater. *Desalination*, 443:198 – 211, 2018. URL https://doi.org/10.1016/j.desal.2018.05.010.

J. S. Stanton, D. W. Anning, C. J. Brown, R. B. Moore, V. L. McGuire, S. L. Qi, A. C. Harris, K. F. Dennehy, P. B. McMahon, J. R. Degnan, and J. K. Böhlke. Brackish groundwater in the United States. *U.S. Geological Survey Professional Paper 1833*, page 185, 2017. URL https://doi.org/10.3133/pp1833.

H. Strathmann. Electrodialysis, a mature technology with a multitude of new applications. *Desalination*, 264(3):268 – 288, 2010. URL https://doi.org/10.1016/j.desal.2010.04.069.

A. T. K. Tran, Y. Zhang, D. De Corte, J.-B. Hannes, W. Ye, P. Mondal, N. Jullok, B. Meesschaert, L. Pinoy, and B. van der Bruggen. P-recovery as calcium phosphate from wastewater using an integrated selectrodialysis/crystallization process. *Journal of Cleaner Production*, 77:140–151, 2014. URL https://doi.org/10.1016/j.jclepro.2014.01.069.

E. Will and J. E. Faust. Irrigation water quality for greenhouse production. *Agricultural Extension Service, The University of Tennessee*, 1999. URL http://trace.tennessee.edu/utk_agexcomhort/5.

N. C. Wright and A. G. Winter. Justification for community-scale photovoltaic-powered electrodialysis desalination systems for inland rural villages in India. *Desalination*, 352:82–91, 2014. URL https://doi.org/10.1016/j.desal.2014.07.035.

N. C. Wright, S. R. Shah, S. E. Amrose, and A. G. Winter. A robust model of brackish water electrodialysis desalination with experimental comparison at different size scales. *Desalination*, 443:27 – 43, 2018a. URL https://doi.org/10.1016/j.desal.2018.04.018.

N. C. Wright, S. R. Shah, S. E. Amrose, and A. G. Winter. A robust model of brackish water electrodialysis desalination with experimental comparison at different size scales. *Desalination*, 443:27–43, 2018b. URL https://doi.org/10.1016/j.desal.2018.04.018.

U. Yermiyahu, A. Tal, A. Ben-Gal, A. Bar-Tal, J. Tarchitzky, and O. Lahav. Rethinking desalinated water quality and agriculture. *Science*, 318(5852):920–921, 2007. URL https://doi.org/10.1126/science.1146339.

Y. Zhang, S. Paepen, L. Pinoy, B. Meesschaert, and B. van der Bruggen. Selectrodialysis: Fractionation of divalent ions from monovalent ions in a novel electrodialysis stack. *Separation and Purification Technology*, 88:191–201, 2012. URL https://doi.org/10.1016/j.seppur.2011.12.017.

A. L. Zydney. Stagnant film model for concentration polarization in membrane systems. *Journal of Membrane Science*, 130(1):275 – 281, 1997. URL https://doi.org/10.1016/S0376-7388(97)00006-9.